

WASP-39b: exo-Saturn with patchy cloud composition, moderate metallicity, and underdepleted S/O

Ludmila Carone¹, David A. Lewis^{1,2}, Dominic Samra¹, Aaron D. Schneider^{3,4}, and Christiane Helling^{1,2}

¹ Space Research Institute, Austrian Academy of Sciences, Schmiedlstrasse 6, A-8042 Graz, Austria
e-mail: Ludmila.Carone@oeaw.ac.at

² Institute for Theoretical Physics and Computational Physics, Graz University of Technology, Petersgasse 16 8010 Graz

³ Institute of Astronomy, KU Leuven, Celestijnenlaan 200D, 3001, Leuven, Belgium

⁴ Center for ExoLife Sciences, Niels Bohr Institute, Øster Voldgade 5, 1350 Copenhagen, Denmark

December 2, 2025, Received September 15, 2996; accepted March 16, 2997

ABSTRACT

Context. WASP-39b is one of the first extrasolar giant gas planet that have been observed within the JWST ERS program. Data interpretation by different retrieval approaches diverge. Fundamental properties that may enable the link to exoplanet formation differ amongst methods, for example metallicity and mineral ratios. The retrieval of these values impact the results for individual element abundances as well as the presence or absence of chemical tracer species. This challenge is eminent for all JWST targets.

Aims. The formation of clouds in the atmosphere of WASP-39b is explored to investigate how inhomogeneous cloud properties (particle sizes, material composition, opacity) may be for this intermediately warm gaseous exoplanet.

Methods. 1D profiles extracted from the 3D GCM expeRT/MITgcm results are used as input for a kinetic, non-equilibrium cloud model. Resulting cloud particle sizes, number densities and material volume fractions are the input for opacity calculations.

Results. WASP-39b's atmosphere has a comparable day-night temperature median with sufficiently low temperatures that clouds may form globally. The presence of clouds on WASP-39b can explain observations without resorting to a high ($> 100\times$ solar) metallicity atmosphere for a reduced vertical mixing efficiency. The assessment of mineral ratios shows an under-depletion of S/O due to condensation compared to C/O, Mg/O, Si/O, Fe/O ratios. Vertical patchiness due to heterogeneous cloud composition challenges simple cloud models. An equal mixture of silicates and metal oxides is expected to characterise the cloud top. Further, optical properties of Fe and Mg silicates in the mid-infrared differ significantly which will impact the interpretation of JWST observations.

Conclusions. WASP-39b's atmosphere contains clouds and the underdepletion of S/O by atmospheric condensation processes suggest the use of sulphur gas species as a possible link to primordial element abundances. Over-simplified cloud models do not capture the complex nature of mixed-condensate clouds in exoplanet atmospheres. The clouds in the observable upper atmosphere of WASP-39b are a mixture of different silicates and metal oxides. The use of constant particles sizes and/or one-material cloud particles alone to interpret spectra may not be sufficient to capture the full complexity available through JWST observations.

Key words. planets and satellites: individual: WASP-39b - planets and satellites: atmospheres - planets and satellites: gaseous planets - planets and satellites: fundamental parameters

1. Introduction

WASP-39b was one of the first extrasolar planets for which the James Webb Space Telescope (JWST) observations were released to the community. Similar to WASP-96b, it was observed in transmission using the NIRSpec instrument as part of the Early Release Science Programme (ERS) (The JWST Transiting Exoplanet Community Early Release Science Team et al. 2022). WASP-39b has a mass of $M_p = 0.28 M_{\text{Jup}}$, a radius of $R_p = 1.27 R_{\text{Jup}}$, an equilibrium temperature of $T_{\text{eq}} \sim 1100$ K, and orbits a G-type star with a period of 4.055 days (Faedi et al. 2011). WASP-96b has a mass of $0.48 \pm 0.03 M_{\text{Jup}}$, a radius of $1.2 \pm 0.06 R_{\text{Jup}}$, an equilibrium temperature $T_{\text{eq}} \sim 1300$ K, and orbits a G-type star with a period 3.4 days (Heller et al. 2014).

The WASP-39b JWST ERS observation, covering the 3 – 5 μm wavelength range, suggest a strong CO_2 absorption feature at 4.3 μm (The JWST Transiting Exoplanet Community Early Release Science Team et al. 2022). Further observations with JWST instruments have also reported the detection of CO_2 (Rustamkulov et al. 2022; Ahrer et al. 2022). Previous observations with HST/WFC3, HST/STIS, and the VLT, as well as recent ob-

servations with several instruments on JWST have ascertained the presence of water, sodium, and potassium in the atmosphere of WASP-39b (Fischer et al. 2016; Nikolov et al. 2016; Wakeford et al. 2018; Rustamkulov et al. 2022; Alderson et al. 2022; Ahrer et al. 2022; Feinstein et al. 2022). Photochemical production has been proposed as the source of the SO_2 detection in the WASP-39b atmosphere (Tsai et al. 2022). The observability of spectral features, in particular the pressure broadened Na and K lines lead Sing et al. (2016) to suggest that the atmosphere of WASP-39b may be relatively cloud free. Fischer et al. (2016) use HST/STIS in combination with the Spitzer/IRAC photometry to suggest a clear-sky WAPS-39b. Their best fit to the data suggest a H_2 dominated atmosphere with either a clear atmosphere of $0.1\times$ to solar metallicity, or a weak haze layer with solar abundances. Wakeford et al. (2018) suggest asymmetric limbs as a possibilities to fit their observations of WASP-39b. Analysis of observations with JWST/NIRCam, JWST/NIRSpec G395H, JWST/NIRSpec PRISM, and JWST/NIRISS, favour a cloudy atmosphere (Rustamkulov et al. 2022; Alderson et al. 2022; Ahrer et al. 2022; Feinstein et al. 2022). Retrieval studies often use assumptions about atmospheric clouds, including

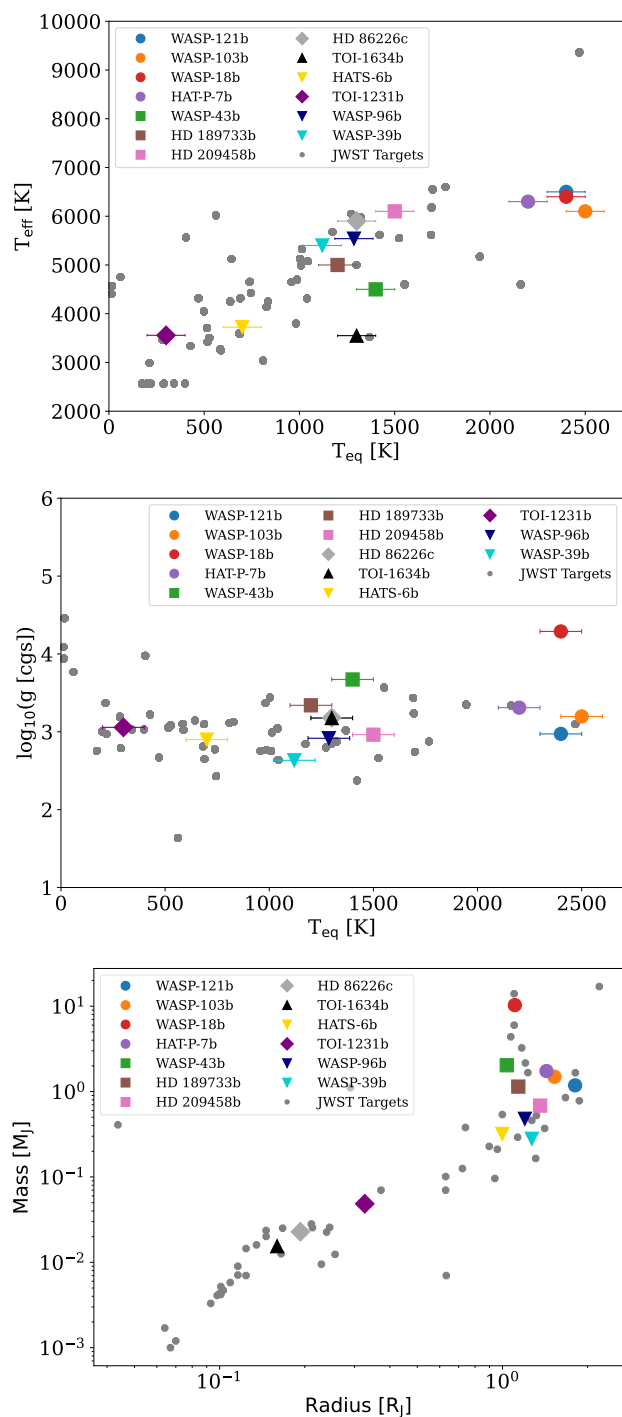


Fig. 1: The JWST ESR targets WASP-39b (light-blue triangle) and WASP-96b (purple triangle) comfortably share the T_{eq} , $\log(g)$ and T_{eff} parameter ranges with the exoplanet subclass of hot Jupiters like HD 189773b. Comparing known exoplanets in the (R_p, M_p) -plane shows both sharing the parameter space with the warm Saturn HATS-6b. The grey symbols indicate the presently known JWST exoplanet targets.

clouds being homogeneous in wavelength (‘grey’ clouds), in composition as well as in particle size (Barstow et al. 2017; Wakeford et al. 2018). These assumptions could be problematic as evidenced by disparate results for WASP-39b and planets of similar mass and temperature ($T_{\text{eq}} \lesssim 1300$ K).

Carone et al. (2021a) studied the atmosphere of WASP-117b which is similar to WASP-39b in mass and radius. A muted water feature was detected in WASP-117b using HST/WFC3. There was no conclusive ($> 3\sigma$) detection of Na and K in the high-resolution VLT/ESPRESSO data. It was shown that the retrieval process can lead to bifurcating results since two models would be consistent with the observations. The first, a 1D, isothermal atmosphere model with a uniform cloud deck and in equilibrium chemistry suggests preference for a high atmospheric metallicity $[\text{Fe}/\text{H}] = 2.58 \pm 0.26$ but clear skies in Bayesian analysis. The data are, however, also consistent with a lower metallicity $\sim 0.37 \times \epsilon_{\text{solar}}$ (ϵ_{solar} - solar metallicity), $[\text{Fe}/\text{H}] < 1.75$ and a cloud deck between $10^{-2.2} \dots 10^{-5.1}$ bar.

Wakeford et al. (2018) report a cloud-free and very high metallicity of more than $100 \times \epsilon_{\text{solar}}$ for WASP-39b based on a combination of HST/WFC3, VLT/FORS2, HST/STIS and *Spitzer* observations. This result is degenerate with C/O ratio and cloud coverage. As was found for WASP-117b, a lower metallicity - more in line with Solar System Saturn of $\sim 10 \times \epsilon_{\text{solar}}$ (Fletcher et al. 2011; Atreya et al. 2016) - can be fitted to the data if a cloud coverage is allowed within the retrieval approach. Further, asymmetrically cloudy limbs would mimic a high metallicity atmosphere if 1D retrieval models are assumed (Line & Parmentier 2016).

Statistical trends in exoplanet atmosphere metallicity suggest that also exoplanets follow a similar metallicity-mass trend as known for the gas planets in the Solar System (Chachan et al. 2019; Welbanks et al. 2019): lower mass gas planets are more metal-rich than more massive gas planet. This trend is also in-line with planet formation models for planets that have migrated in the proto-planetary disk (Schneider & Bitsch 2021; Knierim et al. 2022). Thus, for Saturn-mass objects like WASP-39b, a moderately increased atmosphere metallicity ($10 \times \text{solar}$) similar to Saturn in the Solar System can be expected (Thorngrén & Fortney 2019; Guillot et al. 2022).

This paper addresses the question of cloud formation in the atmosphere of WASP-39b by applying a microphysical model that self-consistently treats the formation of cloud condensation nuclei, their growth to macroscopic particles from multiple condensing species, element depletion, and the feedback of gravitational settling on these processes.

Combining the cloud model with the output of a 3D General Circulation Model (GCM) for the 3D thermodynamic atmosphere structure, shows that the cloud properties vary vertically heterogeneous however they maintain a relatively homogeneous horizontal distribution, in contrast to ultra-hot Jupiters, such as HAT-P-7b or WASP-121b (Helling et al. 2021). The dominant gas phase species after condensation are explored showing that H_2S is less strongly affected by cloud formation and the local thermodynamics than CO_2 . The impact of atmospheric metallicity on cloud formation is assessed, illustrating that high metallicity leads to an increased cloud mass. The potential for using the S/O ratio as a link to planet formation processes is discussed. The potential of using the complex cloud model to link to the currently available observational data for WASP-39b is explored. For WASP-39b, similar to WASP-96b, a reduced mixing efficiency in the cloud model is required to produce a cloud deck between $p_{\text{gas}} = 10^{-2}$ and 5×10^{-3} bar as implied by the observations. The potentially misleading effects of over-simplified cloud parameterisations (for example, constant particle sizes or homogeneous cloud particle composition) is demonstrated.

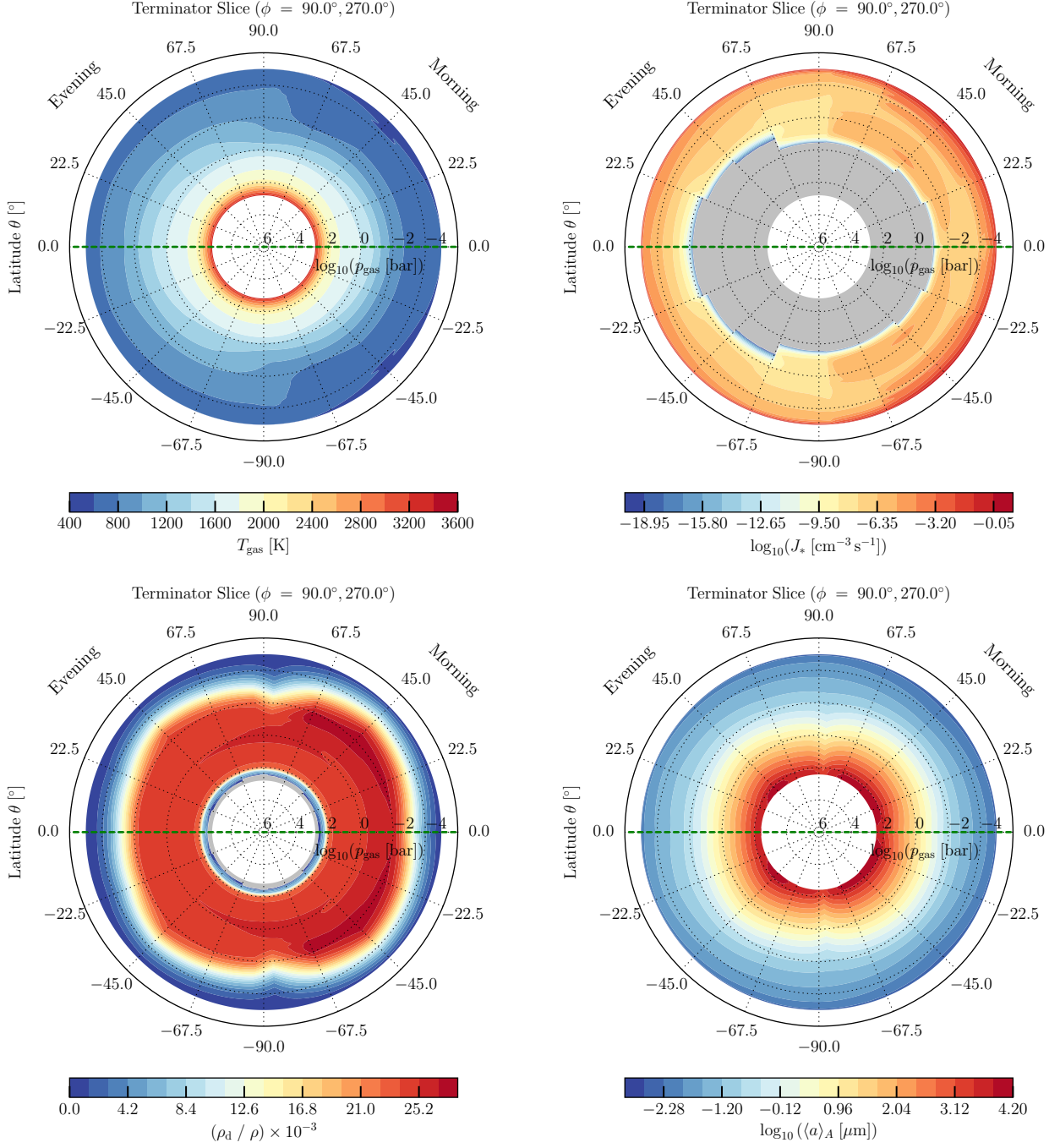


Fig. 2: WASP-39b 2D slices showing atmosphere and cloud structure terminator maps. **Top Left:** Local atmospheric gas temperature and gas pressure (T_{gas} , p_{gas}). **Top Right:** Total nucleation rate, $J_* = \sum_i J_i$ [$\text{cm}^{-3} \text{s}^{-1}$] ($i=\text{TiO}_2, \text{SiO}, \text{NaCl}, \text{KCl}$). **Bottom left:** Dust-to-gas mass ratio ρ_d/ρ . **Bottom right:** Surface averaged mean cloud particle radius $\langle a \rangle_A$ [μm].

2. Approach

The cloud structure on the JWST ERS target WASP-39b is examined by adopting a hierarchical approach similar to works on another JWST ERS target WASP-96b (Samra et al. 2022), the canonical hot Jupiters HD 189733b and HD 209458b (Lee et al. 2015; Helling et al. 2016), and the ultra-hot Jupiters WASP-18b (Helling et al. 2019a) and HAT-P-7b (Helling et al. 2019b; Molaverdikhani et al. 2020). The first modelling step produces

a cloud-free 3D GCM representing WASP-39b. These results are used as input for the second modelling step, which is a kinetic cloud formation model consistently combined with equilibrium gas-chemistry calculations. 120 1D ($T_{\text{gas}}(z)$, $p_{\text{gas}}(z)$, $v_z(z)$)-profiles are utilised for WASP-39b similar to our previous works. $T_{\text{gas}}(z)$ is the local gas temperature [K], $p_{\text{gas}}(z)$ is the local gas pressure [bar], and $v_z(z)$ is the local vertical velocity component [cm s^{-1}].

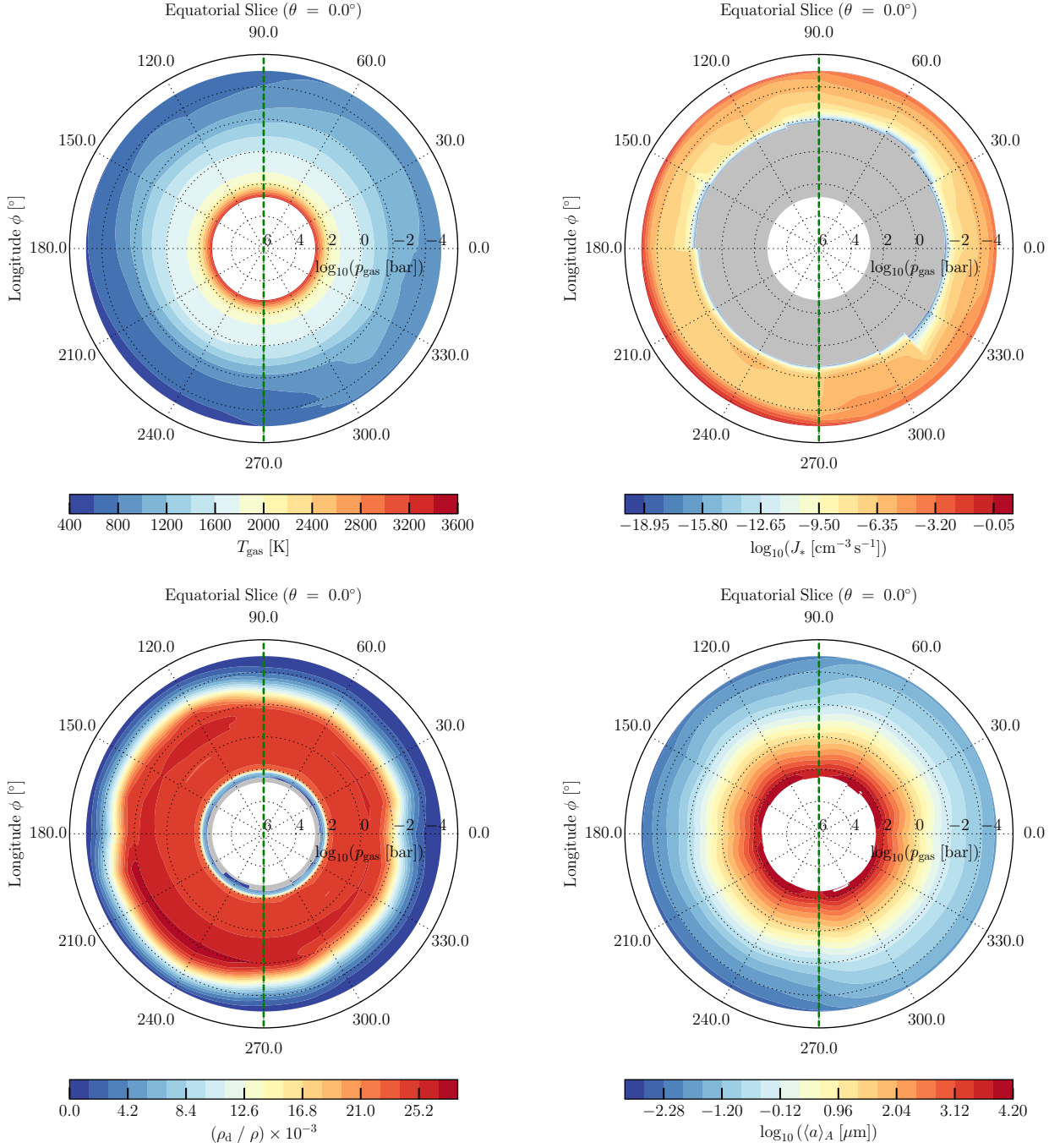


Fig. 3: WASP-39b 2D slices showing atmosphere and cloud structure equatorial maps. **Top Left:** Local atmospheric gas temperature and gas pressure (T_{gas} , p_{gas}). **Top Right:** Total nucleation rate, $J_* = \sum_i J_i$ [$\text{cm}^{-3} \text{s}^{-1}$] ($i=\text{TiO}_2, \text{SiO}, \text{NaCl}, \text{KCl}$). **Bottom left:** Dust-to-gas mass ratio ρ_d/ρ . **Bottom right:** Surface averaged mean cloud particle radius $\langle a \rangle_A$ [μm].

This hierarchical approach is limited by not explicitly taking into account the potential effect of horizontal winds on cloud formation. However, processes governing the formation of mineral clouds are mainly determined by local thermodynamic properties which result from the 3D GCM. The temperature structure may change if the cloud particle opacity is fully taken into account in the solution of the radiative transfer. This may change the precise location of the cloud in pressure space but not the

principle result of clouds forming in WASP-39b. In the following, the individual modelling steps are described in more detail.

3D atmosphere modelling: The 3D GCM expeRT/MITgcm (Carone et al. 2020; Baeyens et al. 2021) is utilised to model WASP-39b. The code was used by Schneider et al. (2022b) to demonstrate that inflation of extrasolar giant gas planets is probably not caused by vertically advected heat. The ex-

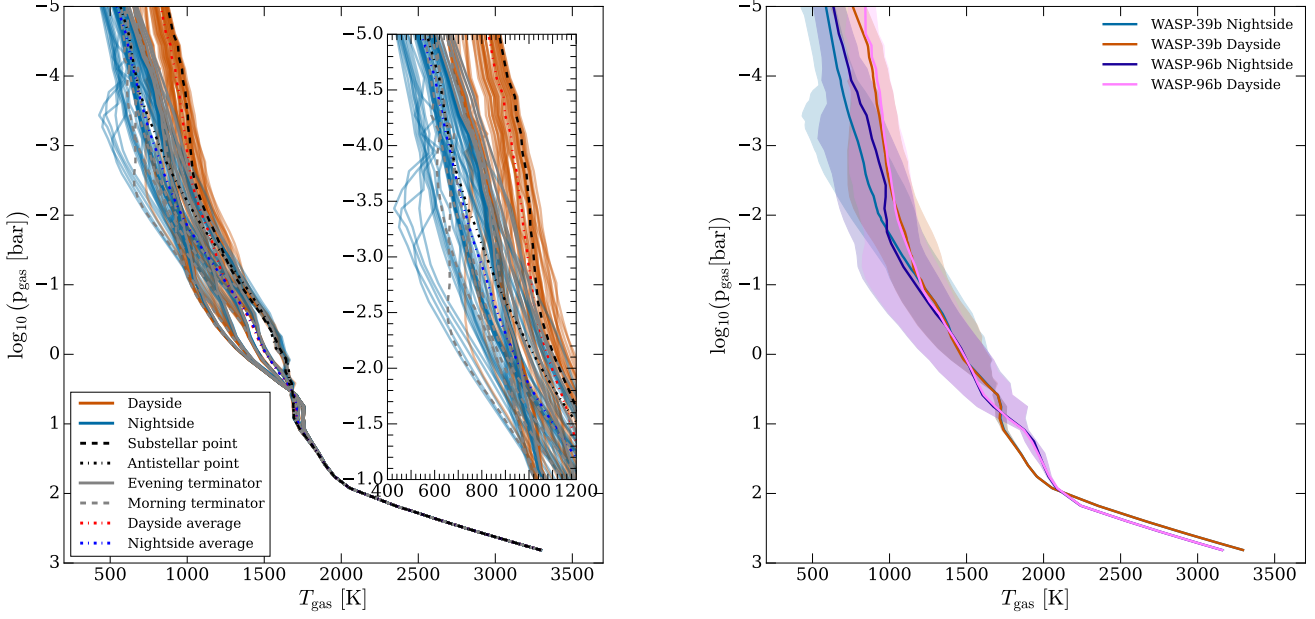


Fig. 4: $(T_{\text{gas}}, p_{\text{gas}})$ - profiles extracted from the 3D GCM in the non-grey version presented in Schneider et al. (2022a). **Left:** The 120 1D profiles extracted from a WASP-39b 3D GCM. The inset highlights the region of the nightside where Rossby vortices form at $\theta \sim \pm 68^\circ$ (see also Fig. A.1) **Right:** WASP-39b and WASP-96b day- and nightside median $(T_{\text{gas}}, p_{\text{gas}})$ profiles with maximum and minimum temperature envelopes. The dayside and the nightside of WASP-96b are on average slightly hotter than WASP-39b.

peRT/MITgcm builds on the dynamical core of MITgcm (Adcroft et al. 2004) and has been adapted to model tidally locked gas giants. Recent extensions in Schneider et al. (2022a) include non-grey radiative transfer coupling. The model parameters used for the GCM, representative of the hot Saturn WASP-39b, are: $R_p = 9.07 \times 10^9$ cm, $P_{\text{rot}} = 4.06$ days, $\log_{10}(g [\text{cm s}^{-2}]) = 2.63$, and the substellar point irradiation temperature $T_{\text{irr}} = 1580$ K or an equilibrium temperature assuming full heat distribution and zero albedo of $T_{\text{eq}} = 1117.4$ K (Eq. 20 Schneider et al. 2022a). The atmosphere of WASP-39b is assumed to have a metallicity of $10 \times \epsilon_{\text{solar}}$. The model is run for 700 days. Additional details for the 3D GCM setup can be found in Table A.1.

Kinetic cloud formation: The kinetic cloud formation model (nucleation, growth, evaporation, gravitational settling, element consumption and replenishment) and equilibrium gas-phase calculations are applied following a similar approach as taken in Helling et al. (2022). The undepleted gas phase element abundances are set to $10 \times \epsilon_{\text{solar}}$ by increasing all element abundances of metals. A constant mean molecular weight¹ of $\mu = 2.4$ is used to reflect the higher value expected compared to a solar abundance H_2/He dominated atmosphere. This constant value is a reasonable assumption given that the thermodynamic structure of the atmosphere does not cause the gas composition to deviate from a H_2 -dominated gas.

In total, 31 ODEs are solved to describe the formation of cloud condensation nuclei ($J_*(z) = \sum_i J_i$, $i = \text{TiO}_2, \text{SiO}, \text{KCl}, \text{NaCl}$) which grow to macroscopic sized cloud particles comprised of a difference condensate species which change depending on the local atmospheric gas temperature and gas pressure.

¹ This value is derived from the specific gas constant R used in the GCM (Table A.1).

The 16 condensate species considered are $\text{TiO}_2[\text{s}]$, $\text{Mg}_2\text{SiO}_4[\text{s}]$, $\text{MgSiO}_3[\text{s}]$, $\text{MgO}[\text{s}]$, $\text{SiO}[\text{s}]$, $\text{SiO}_2[\text{s}]$, $\text{Fe}[\text{s}]$, $\text{FeO}[\text{s}]$, $\text{FeS}[\text{s}]$, $\text{Fe}_2\text{O}_3[\text{s}]$, $\text{Fe}_2\text{SiO}_4[\text{s}]$, $\text{Al}_2\text{O}_3[\text{s}]$, $\text{CaTiO}_3[\text{s}]$, $\text{CaSiO}_3[\text{s}]$, $\text{NaCl}[\text{s}]$, $\text{KCl}[\text{s}]$ which form from 11 elements (Mg, Si, Ti, O, Fe, Al, Ca, S, K, Cl, Na) by 132 surface reactions. The vertical mixing is based on $v_z(z)$ and calculated according to Appendix B.1. in Helling et al. (2022) mimicking a diffusive flux across computational cells.

Deriving cloud properties: In Section 3.2, the clouds are quantified in terms of the surface averaged mean particle size $\langle a \rangle_A$ [μm] of the particles that make up the clouds, their material volume fractions V_s/V_{tot} , and the dust-to-gas mass ratio, ρ_d/ρ which represents the cloud mass load. The surface averaged mean particle size $\langle a \rangle_A$ is defined as

$$\langle a \rangle_A = \sqrt[3]{\frac{3}{4\pi} \frac{L_3}{L_2}}, \quad (1)$$

where L_2 and L_3 are the second and third dust moments (Eq.A.1 in Helling et al. 2020).

In Section 3.3, column integrated properties are discussed. As outlined in previous works (Helling et al. 2020; Helling et al. 2021, 2022) the column integrated total nucleation rate is

$$\int_{z_{\text{min}}}^{z_{\text{max}}} J_{*, \text{tot}}(z) dz [\text{cm}^{-2} \text{s}^{-1}]. \quad (2)$$

It quantifies the total amount of cloud condensation nuclei that form along the atmosphere column. The mass that makes up this column of cloud condensation nuclei is

$$\dot{\Sigma} = \int_{z_{\text{min}}}^{z_{\text{max}}} \sum_i m_i J_{*,i}(z) dz [\text{g cm}^{-2} \text{s}^{-1}], \quad (3)$$

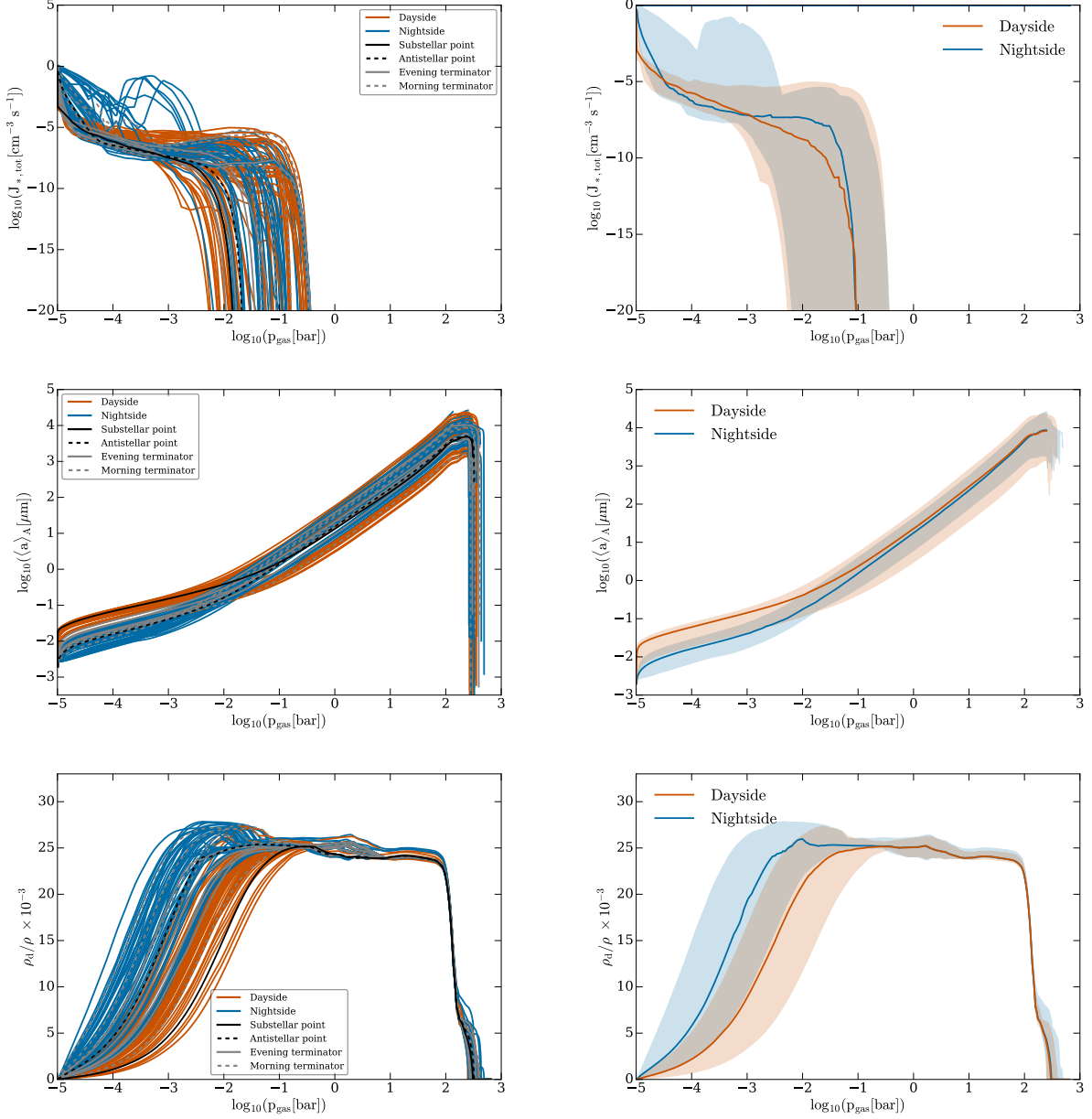


Fig. 5: Microphysical cloud properties of WASP-39 b. **Left column:** Individual 1D profiles which describe the local properties of the cloud. **Right column:** Median dayside and nightside profiles with maximum and minimum planet wide value envelopes. **Top row:** Total nucleation rate $J_{*, \text{tot}}$. **Middle row:** Surface averaged mean cloud particle radius $\langle a \rangle_A$. **Bottom row:** Dust-to-gas mass ratio ρ_d/ρ .

taking into account the four individual nucleation species ($i = \text{TiO}_2, \text{SiO}, \text{NaCl}, \text{KCl}$), with the mass of individual cloud condensation nuclei m_i and their respective nucleation rates $J_{*,i}$.

The column integrated, number density weighted, surface averaged mean particle size is

$$\langle \langle a \rangle_A \rangle = \frac{\int_{z_{\min}}^{z_{\max}} n_d(z) \langle a \rangle_A(z) dz}{\int_{z_{\min}}^{z_{\max}} n_d(z) dz} \quad \text{with} \quad n_d(z) = \frac{\rho(z) L_3(z)}{4\pi \langle a(z) \rangle_A^3 / 3}. \quad (4)$$

The number density of cloud particles (that result from the nucleation rate, Eq. 3) is a weighting factor in Eq. 4 such that the average accounts for differing numbers of particles of different sizes through the atmosphere.

3. Cloud properties on the hot Saturn WASP-39b

The similarity of WASP-39b with WASP-96b in mass and temperature allows to explore the consistency of the cloud model employed here for WASP-39b and in Samra et al. 2022 for WASP-96b. For both planets, ample observational data are available, including JWST data from the ERS programme for WASP-39b, which can be used to further constrain cloud model parameters like vertical mixing. Further, the diverging retrieval results (Sect. 1) of fundamental properties like metallicity for WASP-39b poses a challenge for planet formation and evolution studies, which may be resolved by taking into account cloud formation. Section 3.1 presents the WASP-39b atmosphere thermodynamic structure as a base for the global cloud results in Sect. 3.2 and all following sections. In Sect. 3.2 the global distribution of

the cloud properties is presented which indicates the clouds on WASP-39b are rather homogeneous in nature. It, however, becomes clear in the following sections that, for example, morning and evening terminator differences (Sect. 3.3) and changing material composition (Sect. 3.4) that determine the remaining gas-phase abundances (Sect. 3.5) and the cloud opacity (Sect. 4.3) get lost in simplifications.

3.1. The 3D GCM atmosphere structure

The 3D atmosphere structures of gas giants like WASP-39b and WASP-96b that share a global temperature of $T_{\text{eq}} \sim 1100 \dots 1300\text{K}$ undergo moderate and relatively smooth day-night temperature changes compared to ultra-hot Jupiters with temperatures $T_{\text{eq}} \gtrsim 2000\text{K}$, for example, HAT-P-7b (Helling et al. 2019b). This is shown in Fig. 4 (left) which displays the 120 1D $(T_{\text{gas}}, p_{\text{gas}})$ -profiles which were extracted from the 3D GCM for WASP-39b. The maximum temperature difference between the dayside and the nightside is $\Delta T_{\text{day-night}} \sim 500\text{K}$. The flow of hot gas across the dayside results in the evening terminator being 100-200 K hotter than the morning terminator for a given pressure level where $p_{\text{gas}} \leq 10^{-2}$ bar (see Fig. 2, top left).

Figure 4 (right) encapsulates the complexity of the 3D $(T_{\text{gas}}, p_{\text{gas}})$ -profiles in terms of dayside and nightside median profiles to facilitate comparison or application in retrieval approaches. The maximum error that would occur when only using the median profiles is shown as (red/blue) envelop which represent the maximum deviation from the median amongst all 120 1D profiles. This maximum deviation from the median is determined by a few profiles on the night side that form a vortex cold-trap (Fig. 4, inset). These Rossby vortices appear at latitude $\theta \approx \pm 68^\circ$ as shown in Fig. A.1. This cold-trap is sampled by the profiles $(\phi = -165.0^\circ, \theta = 68.0^\circ)$, $(\phi = -150.0^\circ, \theta = 68.0^\circ)$, $(\phi = -135.0^\circ, \theta = 68.0^\circ)$, $(\phi = -120.0^\circ, \theta = 45.0^\circ)$, $(\phi = -120.0^\circ, \theta = 68.0^\circ)$, and $(\phi = -105.0^\circ, \theta = 68.0^\circ)$ on the nightside at $p_{\text{gas}} \sim 10^{-3.5}$ bar.

The median $(T_{\text{gas}}, p_{\text{gas}})$ -profiles also highlight that WASP-39b and WASP-96b differ only moderately with respect to their atmosphere temperatures. Figure 2 (top left) further demonstrates in 2D terminator slices that the WASP-39b terminator temperature distribution is only very mildly asymmetric within the present 3D GCM modelling domain, again similar to WASP-96b. Since cloud formation is determined by the local thermodynamical conditions in the collision dominated part of any atmosphere, the cloud distribution will be similarly symmetric globally. However, a local cold trap, like the cold Rossby vortices on the night side, may amplify the cloud formation efficiency locally. Such details may be lost when representing the WASP-39b atmosphere profiles in terms of median day and night profiles. It may, however, be reasonable to cast the complexity of physically self-consistent temperature profiles, as used here, in terms of median profiles for better comparison with temperature profiles from retrieval frameworks.

3.2. The global properties of mineral clouds on WASP-39b

Figure 2 (top right) demonstrates where cloud formation is triggered by the formation of cloud condensation nuclei. The local thermodynamic conditions (Fig. 2, top left) trigger the formation of cloud particles generally at pressures $p_{\text{gas}} < 10^{-1}$ bar on the dayside and $p_{\text{gas}} < 10^{-2}$ bar on the nightside. The extension of the global cloud layers reach considerably higher pressures as cloud particles grow and gravitationally settle into the

deeper layers where they evaporate. Hence, the largest particles of $\langle a \rangle_A \sim 10^4 \mu\text{m}$ (Fig. 2, lower right) appear at the cloud base of $p_{\text{gas}} \sim 10^{2.5}$ bar. The dust-to-gas ratio (Fig. 2, lower left) demonstrates the rather symmetric cloud mass load of the WASP-39b atmosphere.

Figure 5 (left) visualises the detailed cloud property results for the total nucleation rate, J_* (top), the surface averaged mean particle size, $\langle a \rangle_A$ (middle), and the dust-to-gas mass ratio, ρ_d/ρ (bottom), for the 120 1D profiles that represent the WASP-39b atmosphere. Figure 5 (right) presents the median and maximum deviation values for the day (orange) and the night (blue) side. The opacity relevant surface averaged mean particle size, $\langle a \rangle_A$ (middle) appears well represented by the median values and the maxima deviations appear very moderate. The nucleation rate, J_* (top), however, has a few order of magnitudes differences between the median profiles for the dayside and the nightside in the upper atmosphere. Furthermore, the spread in deviation away from the nightside median is much larger on the nightside in the upper atmosphere. This affects the cloud particle number density and therefore translates in considerable differences between the median profiles for ρ_d/ρ (bottom). The peak in the maximum deviation from the nightside median profile for J_* , between $p_{\text{gas}} \sim 10^{-4} - 10^{-3.5}$ bar, is due to the few atmosphere profiles that constitute a cold trap due to the Rossby vortices.

Similarly to the cloud model performed for WASP-96b (Samra et al. 2022), also for WASP-39b the cloud properties appear to be relatively horizontally homogeneous for a given hemisphere, except for the Rossby cold traps. The latter will be on the night side and will thus not be observable with transmission spectroscopy. However, to be able to interpret transmission spectra derived by JWST that probe the planetary limbs, particle sizes and material compositions at the morning and evening terminator have to be investigated in more detail. The local thermodynamic conditions of the morning terminator are similar to that of the night side and thus exhibits night side nucleation and the local thermodynamic conditions of the evening terminator are similar to the day side and exhibit correspondingly different nucleation.

3.3. Column integrated properties to reveal differences at the terminators

Column integrated properties (definitions in Sect. 2) provide additional insights at the terminators. The column integrated values are less affected by extreme events like the Rossby vortices which determine the maximum deviations from the median values in Fig. 5. Further, they enable the comparison with results from the ARCIS (Ormel & Min 2019; Min et al. 2020) retrieval framework, which incorporates a self-consistent cloud model, too.

The column integrated nucleation rate mass, $\dot{\Sigma}$, and the column integrated, number density weighted, surface averaged mean particle size, $\langle\langle a \rangle_A\rangle$, are shown in Fig. 6. Figure 6 highlights that differences between the morning and evening terminators of WASP-39b become more apparent in the integrated properties.

The integrated nucleation rates are higher on the nightside with a range of $\dot{\Sigma} \sim 10^{-11.5} \dots 10^{-13.5} \text{g cm}^{-2} \text{s}^{-1}$ compared to the dayside with a range of $\dot{\Sigma} \sim 10^{-13.5} \dots 10^{-15.5} \text{g cm}^{-2} \text{s}^{-1}$. Correspondingly, the values of $\langle\langle a \rangle_A\rangle$ are larger on the dayside, ranging from $\langle\langle a \rangle_A\rangle \sim 10^{-1} \dots 10^{-0.5} \mu\text{m}$, than on the nightside where $\langle\langle a \rangle_A\rangle \sim 10^{-2} \dots 10^{-1} \mu\text{m}$. The evening terminator inherits similar local thermodynamic conditions to the dayside, whereas the morning terminator is similar to the nightside.

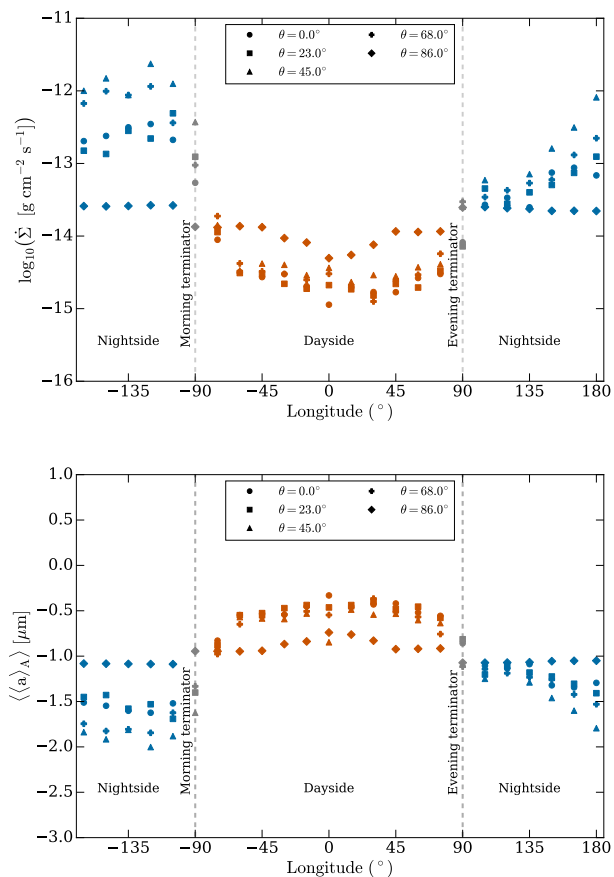


Fig. 6: Column integrated cloud properties for WASP-39b. **Top:** Column integrated mass nucleation rate, $\dot{\Sigma}$. **Bottom:** Column integrated, number density weighted surface averaged mean, particle size, $\langle\langle a \rangle\rangle_A$

Hence, nucleation on the evening terminator is less efficient than the morning terminator ($\dot{\Sigma}_{\text{evening}} < \dot{\Sigma}_{\text{morning}}$) resulting in a larger average particle size at the evening terminator compared to the morning terminator. The evening terminator appears more homogeneous in nucleation efficiency which results into a smaller variation in particle sizes across the limb. Both, $\dot{\Sigma}$ and $\langle\langle a \rangle\rangle_A$ show a moderate variation with latitude. These notable differences in column integrated cloud properties are caused by the moderate differences in the local thermodynamic conditions e.g. the $(T_{\text{gas}}, p_{\text{gas}})$ -profiles.

The values presented in Fig. 6 compare well with the values derived by Min et al. (2020) using ARCiS to perform retrieval on observations of WASP-39b (without JWST data). They derived $\log_{10} \dot{\Sigma} = -12.77^{+3.68}_{-2.93}$ [$\text{g cm}^{-2} \text{s}^{-1}$] from pre-JWST observations, which is consistent with the values that are derived here with self-consistent forward modelling. Similarly, Samra et al. (2022) noted that their column integrated nucleation rate also matched within 1σ ARCiS results for the exo-Saturn WASP-96b. Thus, forward modelling and retrieval can complement each other if retrieved cloud model properties are complex enough.

3.4. Non-homogeneous vertical cloud material composition

WASP-39b's limbs have notable differences in particle size at a given pressure level as result of variations in the local atmospheric density structures. The particle sizes do also strongly

vary in the vertical direction. Therefore, the change of the vertical thermodynamic structure within the atmosphere of WASP-39b causes the cloud properties to be non-homogeneous in size and number, but also in material composition. The changing atmosphere density affects the collisional rates, but the temperature affects the thermal stability (and to a lesser extent the collisional rates) which then results in a changing composition of the cloud particle within the atmosphere. The detailed material compositions of the cloud particles are presented for the substellar (dayside) and the antistellar (nightside) points, as well as for the morning and the evening terminator in the equatorial plane in Sect. 3.4.1. Triggered by the pre-JWST large values ($150 \times \epsilon_{\text{solar}}$) of inferred metallicities for WASP-39b, Sect. 3.4.2 explores the effect of increasing amounts of heavy elements (heavier than He) on the cloud results.

3.4.1. Patchy clouds due to changing thermal stability

The composition of the particles that compose the clouds in the atmosphere of WASP-39b varies throughout the atmosphere due to the changing thermal stability of condensing materials in response to changing local thermodynamic conditions. Figure 7 shows the volume fractions, V_s/V_{tot} , of the individual material condensates at the substellar, antistellar, and equatorial morning and evening terminator. The composition of the cloud layers is shown grouped into silicates ($s=\text{MgSiO}_3[\text{s}]$, $\text{Mg}_2\text{SiO}_4[\text{s}]$, $\text{Fe}_2\text{SiO}_4[\text{s}]$, $\text{CaSiO}_3[\text{s}]$), metal oxides ($s=\text{SiO}[\text{s}]$, $\text{SiO}_2[\text{s}]$, $\text{MgO}[\text{s}]$, $\text{FeO}[\text{s}]$, $\text{Fe}_2\text{O}_3[\text{s}]$), high temperature condensates ($s=\text{TiO}_2[\text{s}]$, $\text{Fe}[\text{s}]$, $\text{FeS}[\text{s}]$, $\text{Al}_2\text{O}_3[\text{s}]$, $\text{CaTiO}_3[\text{s}]$), and salts ($s=\text{KCl}[\text{s}]$, $\text{NaCl}[\text{s}]$) for the morning and evening terminators as 2D slice plots in Fig. 8.

In the upper atmosphere ($p_{\text{gas}} \lesssim 10^{-2}$ bar) there is no clear dominant group of material condensates globally, with both silicates and metal oxides representing the bulk composition and the relative fraction of each varying between profiles. At the morning terminator, silicates and metal oxides represent almost equal fractions of the cloud particle composition with $\sim 50\%$ and $\sim 40\%$ respectively. Over the same pressure region for the evening terminator, the silicates dominate slightly over the metal oxides, each comprising $\sim 60\%$ and $\sim 30\%$ respectively. The remaining $\sim 10\%$ of the cloud particle volume is comprised of high temperature condensates. The dominant silicate condensates are by $\text{MgSiO}_3[\text{s}]$, $\text{Mg}_2\text{SiO}_4[\text{s}]$, and $\text{Fe}_2\text{SiO}_4[\text{s}]$. The dominant metal oxide condensates are $\text{SiO}[\text{s}]$, $\text{SiO}_2[\text{s}]$, and $\text{MgO}[\text{s}]$. The mixed silicate and metal oxide cloud layer extends until the metal oxides become thermally unstable at $p_{\text{gas}} \sim 10^{-3}$ bar for the evening terminator and $p_{\text{gas}} \sim 10^{-2}$ bar for the morning terminator. The thermally unstable material evaporates releasing Mg, Si, and O back into the gas phase which permits further silicate condensation. The increase in the silicate fraction is initially due to an increase in the fraction of $\text{MgSiO}_3[\text{s}]$ from $\sim 16-17\%$ to $\sim 45\%$ of the cloud volume. When $\text{MgSiO}_3[\text{s}]$ evaporates, $\text{Mg}_2\text{SiO}_4[\text{s}]$ becomes the dominant silicate at $\sim 61\%$ of the total cloud particle volume. The maximum contribution of silicates is $\sim 81\%$ occurring by $p_{\text{gas}} \sim 10^{-2}$ bar at the morning terminator and $p_{\text{gas}} \sim 10^{-1}$ bar at the evening terminator. The deepest layers of the atmosphere are dominated by high temperature condensates as all other materials considered here are thermally unstable. The general trends in material composition outlined for the terminators also apply for the substellar and antistellar points. Hence, the clouds on WASP-39b are expected to be patchy in terms of mixed composition in the upper atmosphere, with an extended silicate dominated layer until $p_{\text{gas}} \sim 10^2$ bar.

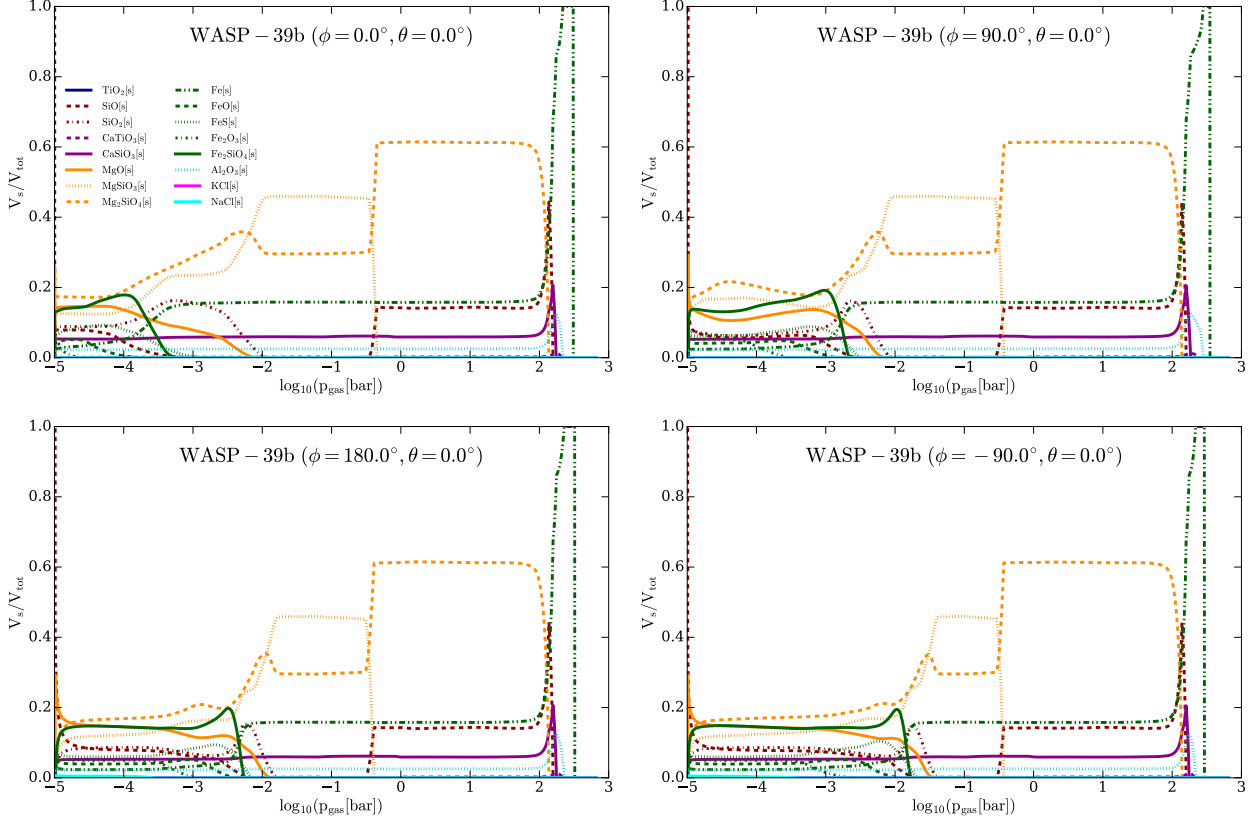


Fig. 7: Volume fractions, V_s/V_{tot} , of individual cloud material condensates at the substellar, antistellar, and equatorial morning and evening terminators for WASP-39b.

3.4.2. Effect of global metallicity on cloud formation

Previous works before JWST data were obtained have reported a wide range of different values for the metallicity of WASP-39b: From solar (Nikolov et al. 2016) to moderately super-solar (Pinhas et al. 2019) to very high values of $151^{+48}_{-46} \times \epsilon_{\text{solar}}$ metallicity (Wakeford et al. 2018).

Notably, the derived atmospheric metallicity changed, depending on cloud model being used for retrieval for the same data. Retrieval with a simple cloud prescription as used by Wakeford et al. (2018) favoured a cloud-free, very high metallicity composition. ARCIS yielded $\sim 15 \times \epsilon_{\text{solar}}$ metallicity (Min et al. 2020) with a more complex cloud model, which is in accordance with recently obtained JWST data (The JWST Transiting Exoplanet Community Early Release Science Team et al. 2022; Rostamkulov et al. 2022; Alderson et al. 2022; Ahrer et al. 2022; Feinstein et al. 2022). For this work $10 \times \epsilon_{\text{solar}}$ metallicity was adopted in the nominal model in accordance of newly obtained JWST data, in contrast to previous work on the similarly warm exo-Saturn WASP-96b, for which solar metallicity was assumed (Samra et al. 2022).

While Min et al. (2020) constrained metallicity for WASP-39b with a cloud model from the retrieval side, it is worthwhile to also explore the impact of different metallicities with forward modelling using a fully microphysical cloud model. The implications of different assumptions of the atmospheric metallicity on the formation of clouds on WASP-39b is explored here. Three different metallicity values are tested for the same equatorial evening terminator ($T_{\text{gas}}, p_{\text{gas}}$)-profile: $1\times$, $10\times$, and $100 \times \epsilon_{\text{solar}}$ abundances. The mean molecular weight, μ , varies for a given ($T_{\text{gas}}, p_{\text{gas}}$)-profile. The values of $\mu = 2.3, 2.4$, and 4.75 are

adopted for the $1\times$, $10\times$, and $100\times\epsilon_{\text{solar}}$ cases, respectively. A value of $\mu = 2.3$ is expected for a solar H_2/He dominated atmosphere. The choice of $\mu = 4.75$ is motivated by equilibrium chemistry calculations for the equatorial evening terminator ($T_{\text{gas}}, p_{\text{gas}}$)-profile using GGChem (Woitke et al. 2018) which show $\mu = 4.73 \dots 4.81$ throughout the atmosphere. The $10\times\epsilon_{\text{solar}}$ case with $\mu = 2.4$ is the same as presented in the previous sections. The change in metallicity is applied only in the cloud formation simulation, therefore, any impact on the ($T_{\text{gas}}, p_{\text{gas}}$)-profile which may arise from a different metallicity is not included here.

The differences in the total nucleation rate ($J_{*,\text{tot}}$), total particle number density (n_d), surface averaged particle size ($\langle a \rangle_A$), and material composition of cloud particles (V_s/V_{tot}) for each case are presented in Fig. 9. The nucleation efficiency increases slightly with increased metallicity, however, the pressure range over which nucleation occurs does not change significantly. The increased availability of condensable elements results in approximately an order of magnitude increase in the total cloud particle number density for each factor of 10 increase in metallicity. In the upper atmosphere, $p_{\text{gas}} \lesssim 10^{-2}$ bar, there is little difference in $\langle a \rangle_A$. At higher pressures, the slightly increased nucleation rate in the upper atmosphere manifests in a slightly smaller $\langle a \rangle_A$ for $p_{\text{gas}} > 10^{-2}$ bar.

The general trend in which condensates dominate the cloud particle composition remains consistent between in the three cases. In general, the upper atmosphere has a 55%, 40%, 15% mix of silicates, metal oxides, and high temperature condensates, respectively. The most significant difference between the three cases is the extent of deep atmosphere ($p_{\text{gas}} \gtrsim 10^{-2.5}$ bar) silicate

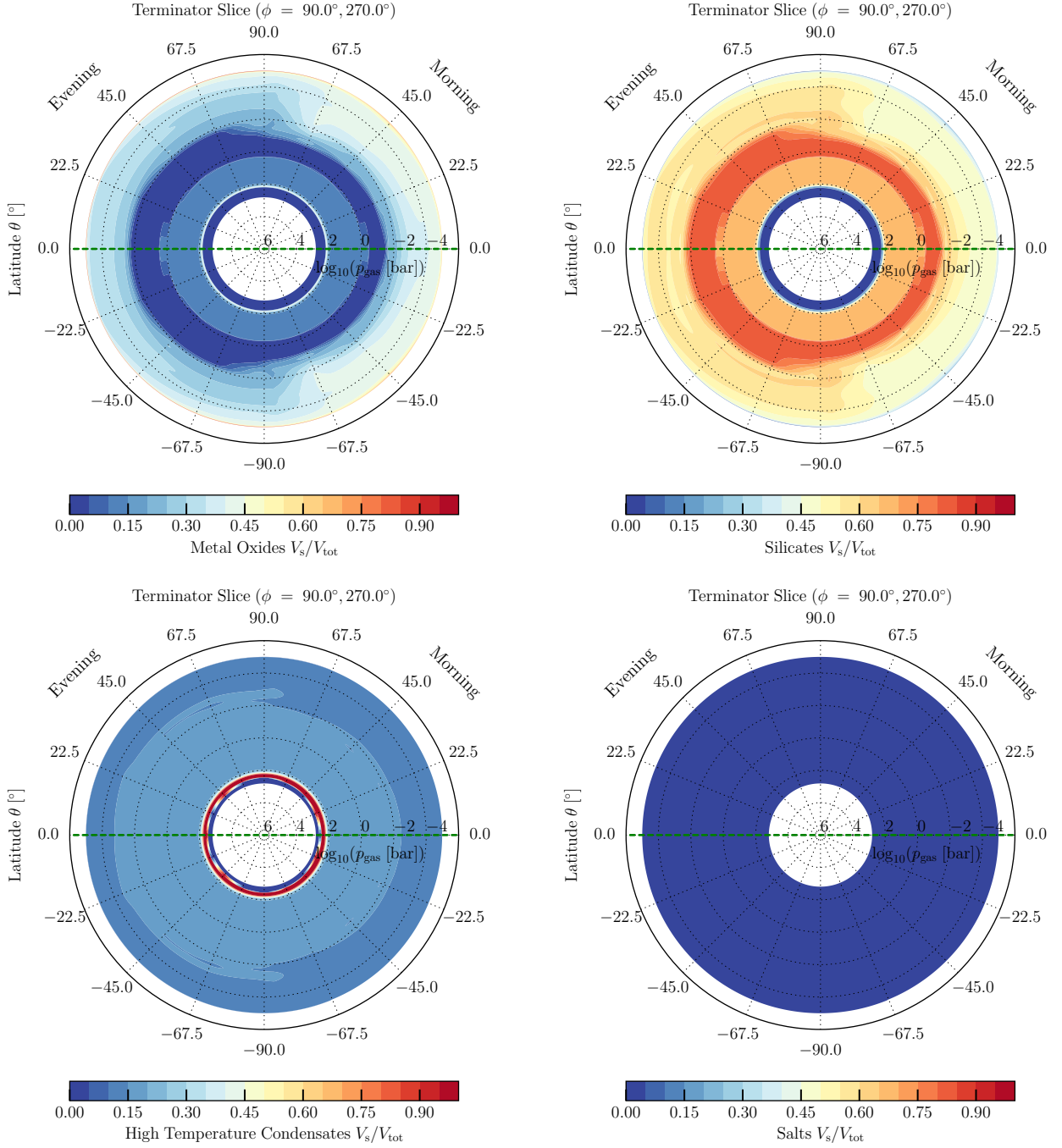


Fig. 8: WASP-39b 2D terminator slices showing the bulk material composition of cloud particles. The materials are grouped as in (Helling et al. 2021): **Top Left:** Metal oxides ($s = \text{SiO}[s], \text{SiO}_2[s], \text{MgO}[s], \text{FeO}[s], \text{Fe}_2\text{O}_3[s]$), **Top Right:** Silicates ($s = \text{MgSiO}_3[s], \text{Mg}_2\text{SiO}_4[s], \text{Fe}_2\text{SiO}_4[s], \text{CaSiO}_3[s]$). **Bottom left** High temperature condensates ($s = \text{TiO}_2[s], \text{Fe}[s], \text{FeS}[s], \text{Al}_2\text{O}_3[s], \text{CaTiO}_3[s]$), **Bottom right** Salts ($s = \text{KCl}[s], \text{NaCl}[s]$).

cloud layer. The increased global abundance of heavy elements increases the thermal stability of the silicate materials at higher pressures. Consequently, the pressure level at which $\text{MgSiO}_3[s]$ evaporates increases from $p_{\text{gas}} \sim 10^{-1.5}$ bar in the $1 \times \varepsilon_{\text{solar}}$ case to $p_{\text{gas}} \sim 10^{-0.5}$ bar and $p_{\text{gas}} \sim 10^{1.5}$ bar in the $10 \times \varepsilon_{\text{solar}}$ and $100 \times \varepsilon_{\text{solar}}$ cases, respectively.

3.5. Atmospheric gas composition

The formation of cloud particles affects the composition of the observed atmospheric gas by depleting those elements that form the respective cloud materials ($\text{Mg}, \text{Si}, \text{Ti}, \text{O}, \text{Fe}, \text{Al}, \text{Ca}, \text{S}, \text{K}, \text{Cl}, \text{Na}$). The most abundant elements (O) are the least affected. Therefore, it is important to explore the composition of the gas phase which results from the formation of clouds.

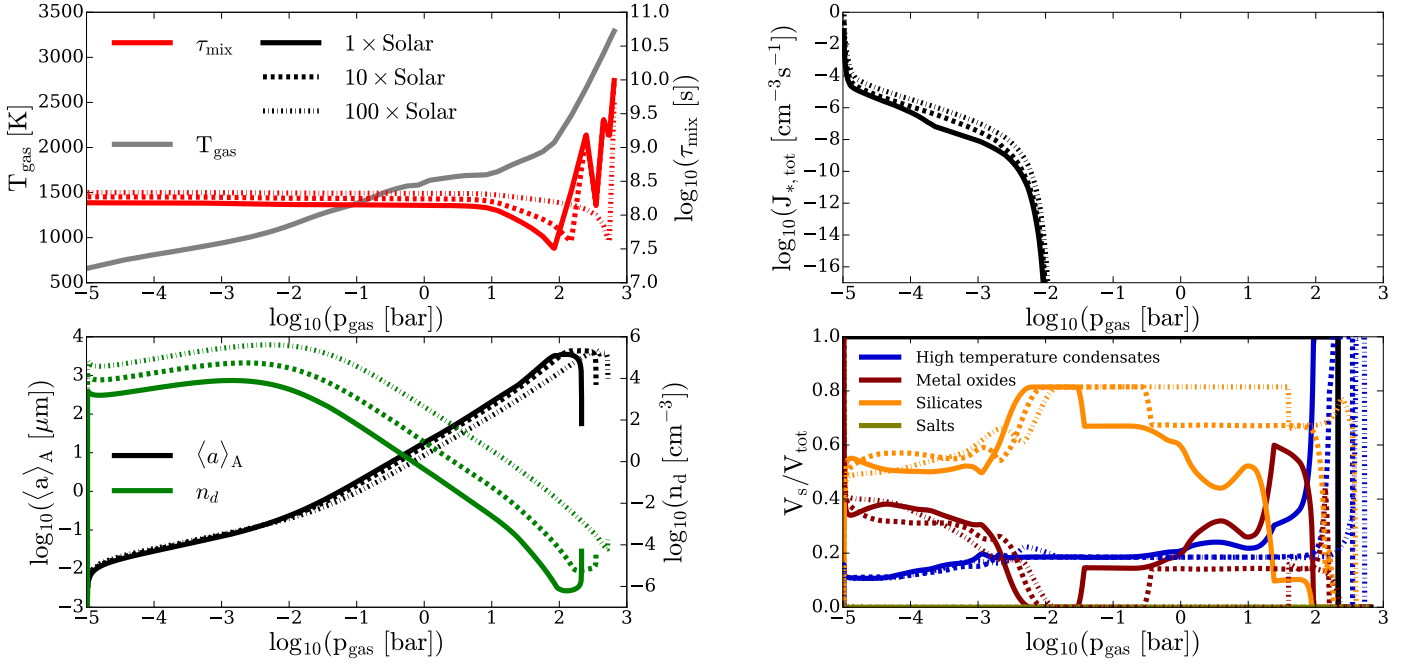


Fig. 9: Metallicity affect on cloud properties shown for the same evening terminator equator ($T_{\text{gas}}, p_{\text{gas}}$)-profile (top left, black line) for WASP-39b. An increased global amount of heavy elements increases the thermal stability of the silicate materials (orange) at higher temperatures where $p_{\text{gas}} > 10^{-2}$ bar. **Top right:** Total nucleation rate, $J_{*,\text{tot}}$ [$\text{cm}^{-3} \text{s}^{-1}$], **Bottom left:** Surface averaged mean particle size (black) and cloud particle number density, n_d [cm^{-3}] (green), **Bottom right:** Material volume fractions, V_s/V_{tot} , for four material groups (high temperature condensates, metal oxides, silicates, salts).

3.5.1. Dominant gas-phase species

In Figure 10 (left) the concentrations of the dominant gas species, excluding H_2/He , for the equatorial morning and evening terminators are shown. The most dominant gas phase species include CO and H_2O , both with concentrations greater than 10^{-3} , as well as H_2S , CO_2 , CH_4 , Na , and K . For most of the species shown the concentrations are generally broadly similar between the two profiles and the concentrations of these species generally do not change significantly through the atmospheres, with the exception of CO_2 and CH_4 . The CO_2 concentration slightly increases by approximately an order of magnitude between $p_{\text{gas}} \sim 10^{-1}$ bar and $p_{\text{gas}} \sim 10^{-5}$ bar. The major exception, however, is CH_4 , with the morning terminator concentration exceeding that of the evening terminator by approximately 3 orders of magnitude in the upper atmosphere ($p_{\text{gas}} \lesssim 10^{-2}$ bar) in equilibrium chemistry. At the cooler gas temperatures, the CO reacts with H_2 to form CH_4 resulting in an increase in the concentration of CH_4 , with the O liberated in this reaction serving to increase the H_2O concentration (Sharp & Burrows 2007).

The concentration of CH_4 at the morning terminator in the upper atmosphere of approximately $n_{\text{CH}_4}/n_{\text{H}_2} \sim 10^{-4}$ is in principle detectable by HST/WFC3 and JWST (e.g. Kreidberg et al. 2018; Carone et al. 2021b). So far, however, methane has not been detected with low resolution spectroscopy for warm exoplanets ($T_{\text{eq}} \lesssim 1200$ K) like WASP-39b. The absence of spectral CH_4 features in these planets suggests that methane abundances may be affected by disequilibrium chemistry (Fortney et al. 2020) via vertical (Moses et al. 2011; Venot et al. 2012) and maybe also by horizontal mixing (Agúndez et al. 2014; Baeyens et al. 2021). Both would quench the amount of CH_4 below the observation limit ($\text{VMR} < 10^{-5}$). Hence, it is reasonable to assume the concentration of CH_4 will be globally homogeneous

and below the detectability threshold. Thus, CH_4 is not included as an opacity species in Sect. 4.2.

Figure 10 (right) compares the concentrations of the dominant gas phase species at the evening terminator between the cloud model and the atmosphere with equilibrium chemistry but without condensation. The concentrations of each species do not differ significantly due to the element depletion associated with the cloud formation.

3.5.2. The role of sulphur in clouds

Elements such as K , Na , and Cl are not significantly affected by cloud formation because their possible condensate materials are thermally unstable in the atmosphere of WASP-39b. In addition, the formation of sulphur-containing materials is considerably less favoured in comparison to the Fe/Mg -containing silicates. Figure 5 in Helling (2019) demonstrates that materials like $\text{S}[\text{s}]$, $\text{MgS}[\text{s}]$, and $\text{FeS}[\text{s}]$ would reach a sweet spot of maximum volume contribution of $\sim 15\%$ when $\text{C}/\text{O} = 0.99 \dots 1.10$ and if the sulphur abundance is enriched above the solar value for a $T_{\text{eff}} = 1200$ K exoplanet. Mahapatra et al. (2017) (Table 3) demonstrate that $\text{FeS}[\text{s}]$ would contribute with $< 1\%$ to cloud particle in gas giants and with $< 10\%$ in hot rocky planets like 55 Cnc e. If sulphur compounds do not condense, the sulphur needs to remain in the gas phase of exoplanet atmosphere. Therefore, the S/O ratio would remain near-solar as demonstrated in Fig. 4 in Helling (2019). This negative result for the role of sulphur contributing to the cloud mass in exoplanets (and brown dwarfs) is supported by similar findings for AGB stars. The study of post-AGB stars shows a lack of sulphur depletion (Waelkens et al. 1991; Reyniers & van Winckel 2007) which is interpreted as a lack of sulphure condensation into dust grain in AGB stars (Danilovich et al. 2018).

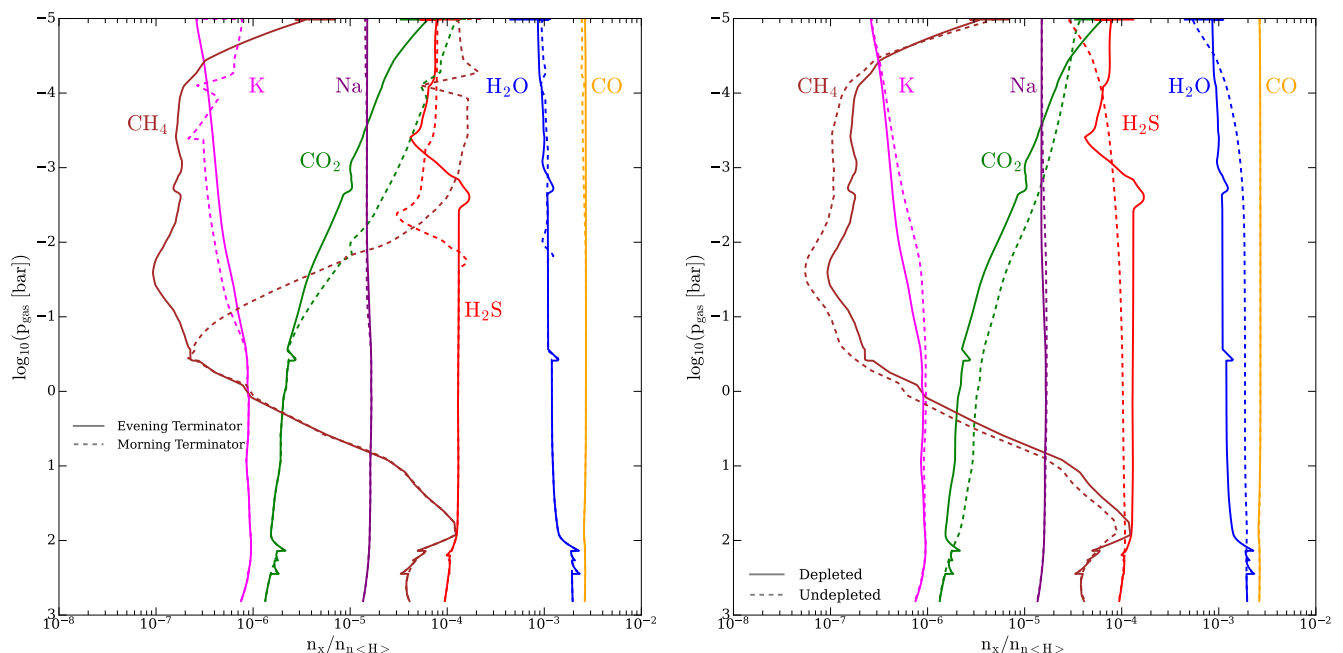


Fig. 10: Gas phase concentrations ($n_x/n_{<H>}$) for selected molecules at the WASP-39b equatorial morning and evening terminators in chemical equilibrium. **Left:** Comparing morning and evening terminator. **Right:** Comparing results for depleted (after cloud formation) and undepleted element abundances at the equatorial evening terminator.

AGB stars, which undergo strong condensation events (dust formation), enrich the ISM for the next generation of stars and planets to form. Sulphur, is however, not nucleosynthesised in AGB stars but rather in type II supernovae (Colavitti et al. 2009; Perdigon et al. 2021), and is the 10th most abundant element in the Universe, as well as an important element for life on Earth. Oxygen-rich AGB stars are observed to have SO and SO₂ (Danilovich et al. 2020) but H₂S is most likely not a parent molecule since it decays rapidly (Danilovich et al. 2016). H₂S has been found in high-mass loss oxygen-rich stars and is argued to account for a significant fraction of the sulphur abundance in these objects (Danilovich et al. 2017).

Gobrecht et al. (2016) point out also the chemical link between CS, CN, SH and H₂S in carbon-rich AGB stars. Here, SH can combine with O to SO which further may form SO₂; this would also be relevant for oxygen-rich environments or the upper exoplanet atmospheres where photochemistry enables to formation of CS and CN. However, the SH reservoir may be depleted through the formation of H₂S such that it indirectly affects the presence of SO and SO₂. The SH/H₂S chemistry is further dictating the formation of CS and CN which then may continue to form HCN (their Eqs. 5 to 16). The research question is therefore which gas-phase constituent holds the sulphur reservoir if sulphur is not depleted by dust formation in AGB stars or in cloud particles in extrasolar planets / brown dwarfs. **Recently**, Tsai et al. (2022) suggested that H₂S is a precursor molecule which gives rise to SO₂ on WASP-39b via gas-phase non-equilibrium in combination with a solar element overabundance of $10 \times \epsilon_{\text{solar}}$.

To gather a first impression of the exoplanet sulphur reservoir, the most abundant sulphur-binding gas species in the WASP-39b atmosphere, H₂S, is included into the comparison of major gas species in Fig. 10. These are the gas species for which a radiative transfer solution is presented to fit the observational date for WASP-39b in Sect. 4.2.

3.5.3. Mineral ratios Si/O, Mg/O, Fe/O, S/O, C/O

The Si/O, Mg/O, Fe/O, S/O and C/O element abundance ratios for the equatorial morning and evening terminator points are shown in Fig. 11. The cloud formation process reduces the abundances of Si, Mg, and Fe by several orders of magnitude in comparison to oxygen. The reduction is seen for both the morning and evening terminators as cloud formation occurs at both points, however, the morning terminator abundances are reduced more than the evening terminator. The maximum difference in the element ratios between the two terminator points is approximately 1 order magnitude occurring over a pressure range of $p_{\text{gas}} \leq 10^{-2} - 10^{-1}$ bar.

No substantial reduction is seen for sulphur which confirms previous results (Mahapatra et al. 2017; Helling 2019). This indicates that potential reaction partners Fe, Mg, Si are stronger bound by other materials and leads to the conclusion that sulphur gas species may provide means to determine the primordial abundances and hence, to link to planet formation processes. This finding is relevant for all exoplanets.

In contrast to the other element ratios, in regions of cloud formation the C/O is increased from the solar C/O = 0.54 as the oxygen is depleted from the gas phase. The maximum value of C/O ~ 0.75 occurs where $p_{\text{gas}} = 10^{-3}$ bar in the upper atmosphere. In Figure 11 (bottom), the equatorial terminator C/O of WASP-39b is compared to that of the reduced mixing efficiency case of WASP-96b from (Samra et al. 2022). The C/O ratio for WASP-96b drops to C/O ~ 0.31 for both the equatorial morning and evening terminators at $p_{\text{gas}} \sim 10$ bar due to the evaporation of Mg₂SiO₄[s] resulting from the increased gas temperature (see Figs. 2 and 3 in Samra et al. (2022)). The reduced mixing efficiency serves to maintain the sub-solar C/O at this pressure level as the oxygen is not efficiently removed from the evaporation edge of the cloud base.

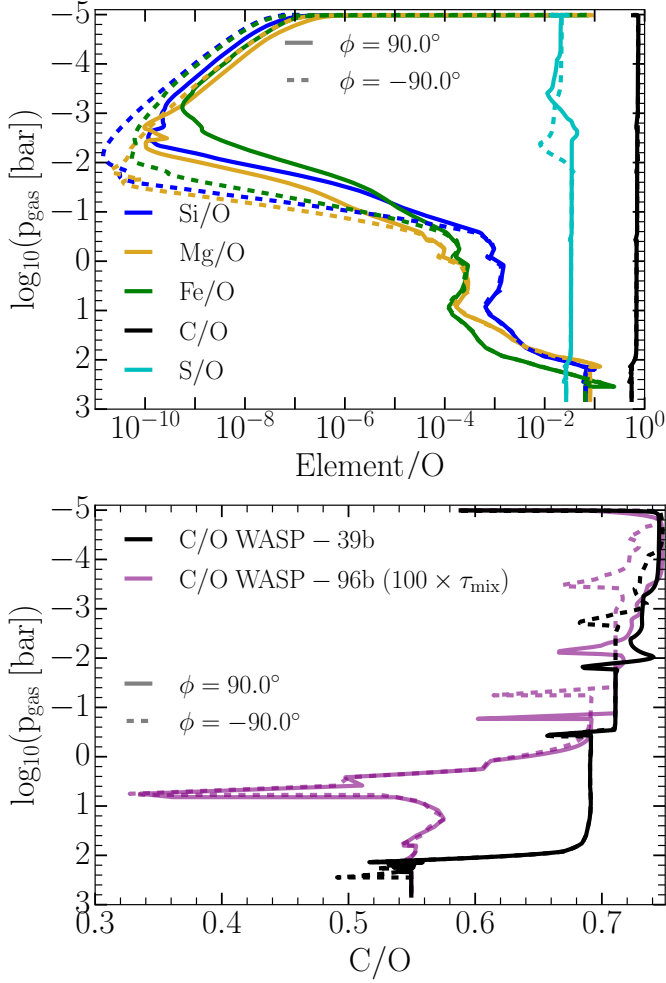


Fig. 11: Gas phase element abundance ratios, for equatorial morning ($\phi = -90.0$, dashed lines) and evening ($\phi = 90.0$, solid lines) terminators. **Top:** The mineral ratios Si/O, Mg/O, Fe/O, S/O, and C/O for WASP-39b. **Bottom:** C/O for both WASP-39b and WASP-96b.

4. The value of simplistic cloud models for observations

Cloud models of varying complexity are used to represent observational data for extrasolar planets. The self-consistent, complex cloud model used in this work yields detailed cloud properties. In atmosphere retrievals, more simplified cloud models in form of a grey cloud prescription is generally used. In this section, both cloud model approaches are applied to understand how the complex cloud model can aid atmosphere retrieval to realise the full potential of JWST observational data. Section 4.1 identifies two distinct wavelength regimes longer and shorter than $\sim 4 \mu\text{m}$ based on the disperse, mixed material cloud results from our kinetic model. Section 4.2 presents a synthetic spectrum for WASP-39b for $\lambda \lesssim 4 \mu\text{m}$ where the cloud may be reasonably well represented by a grey opacity, and Sect. 4.3 discusses the effect of a homo-disperse, homo-material cloud on the cloud opacity which is particularly strong for $\lambda > 4 \mu\text{m}$.

4.1. Disperse, mixed material cloud opacity

Following Helling et al. (2022) and Samra et al. (2022), the atmospheric gas pressure, p_{gas} , is explored where the cloud reaches optical depth $\tau(\lambda) = 1$ as function of wavelength, λ .

The optically thick pressure level aligns with the cloud top pressure which many of the simple grey cloud deck approaches use for fitting spectra. Further, the pressure level at which the clouds become optically thick is a result of the complex cloud model.

Figure 12 demonstrates how the $\tau(\lambda) = 1$ pressure level changes with wavelength if the cloud opacity is calculated using the full microphysical cloud model for WASP-39b as presented in Sect. 3. The optically thick cloud pressure level, $p_{\text{gas}}(\tau(\lambda) = 1)$, is the result of the varying composition, particle size, and number density of cloud particles with pressure. Two distinct wavelength regimes may be identified in Fig. 12: $\lambda < 4 \mu\text{m}$ with no solid-material spectral features but a slope, and $\lambda > 4 \mu\text{m}$ where solid-material spectral features occur.

For $\lambda < 4 \mu\text{m}$, $p_{\text{gas}}(\tau(\lambda) = 1)$ varies by ~ 1.5 orders of magnitude in the wavelength bands that are accessible by HST/WFC3, HST/STIS, VLT/FORS2, JWST/NIRSpec, JWST/NIRCam and future missions like PLATO and Ariel. The pressure range $p_{\text{gas}} \sim 10^{-4.5} \dots 10^{-3}$ bar that is probed at these wavelengths is characterised by cloud particles made of a mix of materials as shown in Table 1. The dominating materials are Mg/Si/O and Fe/Si/O silicates with inclusions from various materials, including further iron compounds like Fe[s] and FeS[s].

For $\lambda > 4 \mu\text{m}$, the pressure range $p_{\text{gas}} \sim 10^{-3}$ bar is probed. This coincides, for the substellar point and evening terminator profiles, with chemically very active regions of the atmosphere, namely where the iron-silicates (for example, $\text{Fe}_2\text{SiO}_4[\text{s}]$, $\text{MgO}[\text{s}]$ and $\text{SiO}_2[\text{s}]$) become thermally unstable and evaporate. Instead, Fe[s], $\text{SiO}_2[\text{s}]$, $\text{Mg}_2\text{SiO}_4[\text{s}]$ and $\text{MgSiO}_3[\text{s}]$ increase their respective volume fractions considerably. This is the reason for the increase in the optical depth of the clouds for only the substellar point (between $\lambda = 4 \dots 8 \mu\text{m}$). Therefore, assuming cloud particles observed at these wavelengths are made of only silicates is questionable.

While the assumption of uniform cloud composition is called into question here, the concept of optical depth $\tau = 1$ is still useful to compare between the complex models, observational data and cloud parameterisation.

4.2. Synthetic transmission spectra of WASP-39b

A first exploration of the available observational data for WASP-39b for $\lambda < 5 \mu\text{m}$ is undertaken with the current, publicly available data, using a grey cloud model for the evening and morning terminator, respectively to derive insights between our complex cloud model and observations (Fig. 13). The synthetic spectra shown in Fig. 13 are computed using *petitRADTRANS* (Mollière et al. 2019) for the GCM ($T_{\text{gas}}, p_{\text{gas}}$)-profile for the equatorial morning and evening terminators, and their respective cloud-depleted gas-phase concentrations (see Fig. 10). The line opacities used for the spectra are CO (Rothman et al. 2010), CO_2 (Yurchenko et al. 2020), H_2O (Rothman et al. 2010), H_2S (Az-zam et al. 2016), Na (Allard et al. 2019), and K (Allard et al. 2016). A simple grey cloud deck is applied to both terminators separately. The synthetic spectra are compared to both pre-JWST observations and all the four different pipeline reduction of the JWST observations from The JWST Transiting Exoplanet Community Early Release Science Team et al. (2022). Systematic effects that lead to offsets between data make it difficult to com-

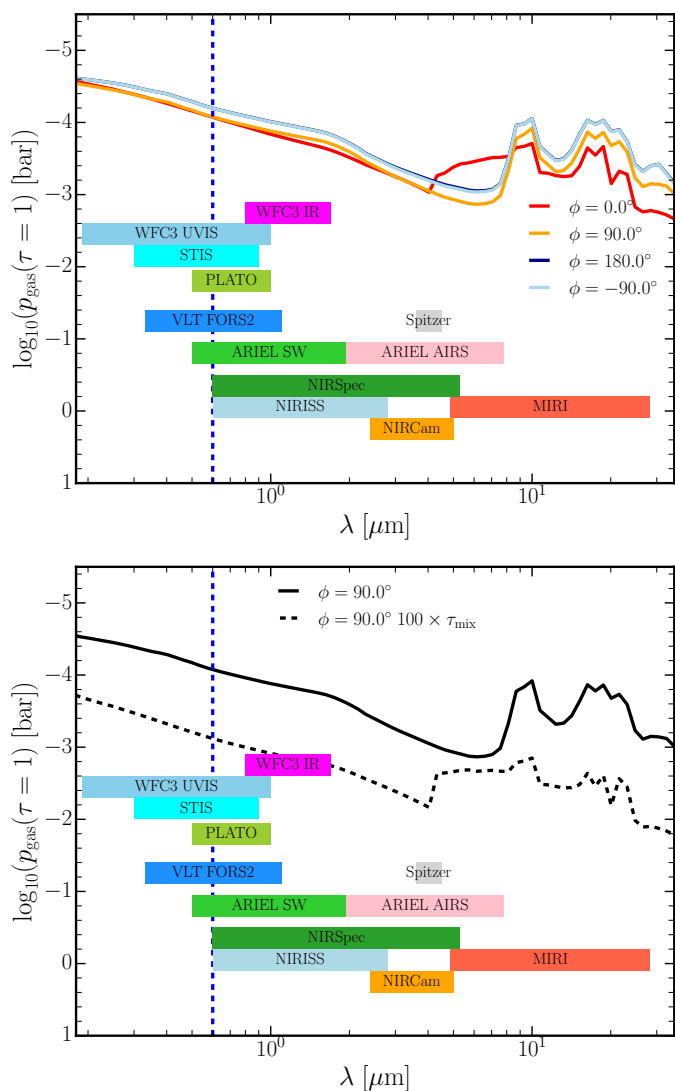


Fig. 12: WASP-39b pressure levels, $p_{\text{gas}}(\tau(\lambda) = 1)$ [bar], at which the atmosphere becomes optically thick due to cloud opacity. **Top:** for the substellar point ($\phi = 0^\circ$, red), anti-stellar point ($\phi = 180^\circ$, dark blue) and the equatorial morning ($\phi = -90^\circ$, light blue) and equatorial evening terminator ($\phi = 90^\circ$, yellow). **Bottom:** for the equatorial evening terminator compared to the same profile but with the mixing timescale $100 \times \tau_{\text{mix}}$. The dashed vertical blue line is the location of Na, coloured bars show wavelength ranges of various instruments.

pare observations from different telescopes. Here, this effect was taken into account by adding 100 - 150 ppm for individual data sets to achieve best fit with the model. *Spitzer* data was treated as suggested in The JWST Transiting Exoplanet Community Early Release Science Team et al. (2022).

The grey cloud model produces generally a good fit with the data available for $\lambda = 0.3 \dots 5 \mu\text{m}$, but is unable to reproduce the slope in the optical which is associated with small cloud particles. The qualitative impact of the cloud opacity can be estimated by examining the parameter $x = 2\pi r/\lambda$, where r is the radius of a spherical cloud particle and λ is the observation wavelength. For $x \ll 1$ Rayleigh scattering is the dominant. Using Fig. 6 as a guide, taking $r \sim \langle a \rangle_A \sim 10^{-1.5} \mu\text{m}$ (representative of the morning terminator) and an observing wavelength of $\lambda = 0.3 \mu\text{m}$ yields a value of $x \approx 0.66$, hence, a Rayleigh scattering slope

would be expected in the optical wavelength regime based on the complex cloud model (see Fig. 12). Figure 5 shows that the population of cloud particles is expected to be smaller than the column integrated value in the upper atmosphere, and thus supports the expectation of an optical slope.

The location of the grey cloud enables another comparison to results from the complex cloud model. Grey cloud decks at $p_{\text{gas}} \sim 10^{-2}$ bar and $p_{\text{gas}} \sim 5 \times 10^{-3}$ bar for the morning and evening terminators, respectively, appear to reproduce the pressure broadening required for the Na line in Fig. 13. There is good agreement between both the synthetic terminator spectra and the observed CO_2 feature at $4.3 \mu\text{m}$, and a reasonable agreement with the observed H_2O features. New work of Alderson et al. (2022); Rustamkulov et al. (2022); Ahrer et al. (2022); Tsai et al. (2022) derive a cloud deck between $3 \times 10^{-4} \dots 10^{-2}$ bar qualitatively agreeing with the range of cloud decks derived here. These authors further noted that varying vertical opacity contribution is required. Horizontal differences in cloud coverage between the limbs is also mentioned as a possibility. As has been noted in Section 3.3, average cloud particle sizes can indeed differ between morning and evening terminators.

In Section 3.5, it was shown that H_2S may be present in chemical equilibrium in significant quantities for WASP-39b. Thus, H_2S was included as an additional opacity source, but no clear impact on the simulated spectrum could be found for $\lambda < 5 \mu\text{m}$. However, other molecules for which H_2S is a precursor may impact observations (Zahnle et al. 2009) as was discussed for AGB stars (see Sect. 3.5.2). The important role of H_2S and sulphur chemistry in WASP-39b has been recently confirmed by Tsai et al. (2022) who present a photochemical pathway from H_2S to explain the recent detection of SO_2 .

The inferred cloud deck pressure level from the complex cloud model can be derived for the Na feature at $\lambda \sim 0.6 \mu\text{m}$ that lies in the optical slope region (Fig. 12). The cloud deck is slightly higher in the atmosphere at $p_{\text{gas}} \sim 10^{-4.4}$ bar for the morning terminator than the evening terminator at $p_{\text{gas}} \sim 10^{-4.2}$ bar. The width of the sodium feature seen in observations suggests, similar to WASP-96b, that the actual cloud deck must be deeper in the atmosphere than shown in Fig. 12. This also agrees with the synthetic spectra fits, which require a deeper cloud deck, namely $p_{\text{gas}} \sim 10^{-2} \dots 5 \times 10^{-3}$ bar, to match observations.

To apply the lessons learned from WASP-96b to WASP-39b, it has to be taken into account that for WASP-96b solar metallicity is assumed whereas for WASP-39b a higher metallicity of 10 times solar is assumed. Samra et al. (2022) illustrate in their Fig. 5 that an enhanced atmosphere metallicity of $10 \times \epsilon_{\text{solar}}$ raises the cloud deck to higher altitudes by almost half an order of magnitude for their models of WASP-96b. They show that the altitude of the cloud deck is reduced by an order of magnitude when the mixing efficiency is reduced by a factor of 100. For WASP-39b, hence, the location of the grey cloud deck required to fit the evening terminator spectrum is broadly consistent with a required factor of $\sim 100 \times$ reduction in mixing efficiency (compare to Fig. 12, bottom). Further the cloud deck for WASP-39b is slightly higher compared to WASP-96b which can be entirely explained by its 10 times higher metallicity. Thus, the cloud model is capable of meeting observations of both planets, by adjusting only one factor: vertical mixing.

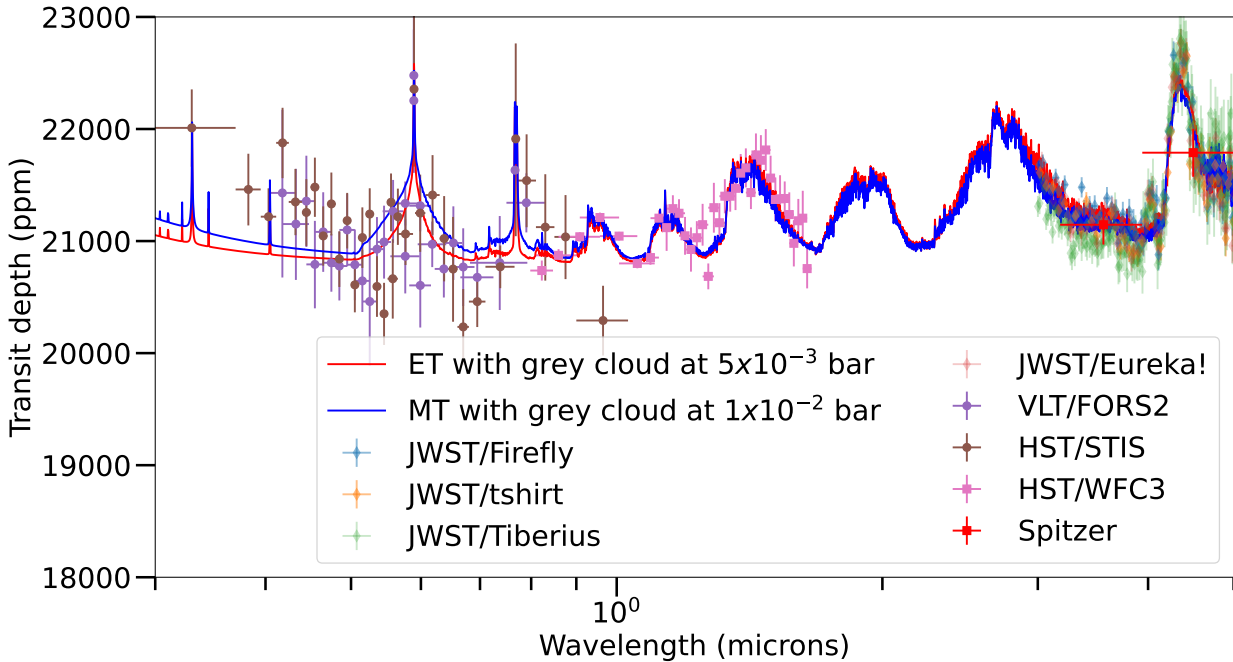


Fig. 13: Synthetic spectra for the equatorial morning and evening terminators of WASP-39b compared to both pre-JWST and JWST observation for $\lambda = 0.3 \dots \sim 5.0 \mu\text{m}$, computed with *petitRADTRANS*. Opacities are considered using the concentrations of the dominant gas phase species output from the kinetic cloud model (H_2O , CO_2 , CO , H_2S , Na , K)

4.3. The effect of over-simplification

It has been shown here that clouds are expected to form in WASP-39b given its temperature of $T_{\text{eq}} \sim 1100 \text{ K}$. A higher cloud mass is expected in WASP-39b compared to WASP-96b because a higher metallicity is assumed. Thus, retrieval approaches that treat atmosphere metallicity and cloud formation as competing processes, when in reality they are intrinsically related may lead to unrealistically high metallicity values (Sect. 3.4.2). Further, cloud formation in the temperature range of $T_{\text{eq}} \sim 1200 \text{ K}$ always tends to raise the C/O ratio in the remaining gas phase due to the silicate and metal oxides removing oxygen (see e.g. Helling et al. 2022). Here, assuming a solar C/O ratio, the observed C/O ratio in the gas phase can be raised to $\text{C/O} \sim 0.7$ (Fig. 11). Thus, again, treating C/O ratios and cloud formation as unrelated to each other, may result in unrealistically low C/O ratios. Retrievals thus tend to produce diverging results with respect to the metallicity and the C/O in exoplanet data interpretation. However, it is challenging to find the optimal degree of simplifications for complex processes like cloud formation.

Again, $p_{\text{gas}}(\tau(\lambda) = 1)$ is used as a tool to demonstrate how assumptions like constant cloud particle sizes and homogeneous cloud particle composition may bias retrieval results. Figure 12 illustrates why the use of over-simplified cloud models is problematic: the cloud particles in the optically thin region (above $p_{\text{gas}}(\tau(\lambda) = 1)$) are highly mixed, with no single condensate species contributing more than $\sim 20\%$.

At different wavelength ranges, different pressure level and thus different cloud materials are probed. This is readily apparent for the substellar point, which shows an excess in cloud opacity between 5 and 8 micron (Fig. 12). Furthermore, as described in Section 4.2 the cloud top of grey clouds needs to be between $p_{\text{gas}} = 10^{-2} \dots 5 \times 10^{-3} \text{ bar}$ in order to fit the Na line pres-

sure broadening. In the case of such a deeper cloud top, a different cloud composition becomes visible by observations: a mixed composition of $\text{MgSiO}_3[\text{s}]/\text{Mg}_2\text{SiO}_4[\text{s}]$ ($\sim 45\%$ and $\sim 30\%$ respectively) at morning terminator. Similarly, lowering the cloud top will allow different local gas-phase chemistry to be probed.

Table 1: Material volume fractions, V_s/V_{tot} , for the evening terminator WASP-39b clouds in decreasing order where $p_{\text{gas}} \approx 2 \times 10^{-4} \text{ bar}$ representing where the cloud regions becomes optically thin.

material	V_s/V_{tot}
$\text{Mg}_2\text{SiO}_4[\text{s}]$	$\sim 19\%$
$\text{MgSiO}_3[\text{s}]$	$\sim 16\%$
$\text{Fe}_2\text{SiO}_4[\text{s}]$	$\sim 16\%$
$\text{MgO}[\text{s}]$	$\sim 13\%$
$\text{FeS}[\text{s}]$	$\sim 7\%$
$\text{SiO}_2[\text{s}]$	$\sim 7\%$
$\text{SiO}[\text{s}]$	$\sim 6\%$
$\text{FeO}[\text{s}]$	$\sim 5\%$
$\text{CaSiO}_3[\text{s}]$	$\sim 5\%$
$\text{Fe}[\text{s}]$	$\sim 3\%$
$\text{Al}_2\text{O}_3[\text{s}]$	$\sim 2\%$
$\text{Fe}_2\text{O}_3[\text{s}]$	$\sim 1\%$
$\text{TiO}_2[\text{s}]$	$< 0.1\%$ (Trace)
$\text{CaTiO}_3[\text{s}]$	$< 0.1\%$ (Trace)
$\text{NaCl}[\text{s}]$	None
$\text{KCl}[\text{s}]$	None

How oversimplified cloud models effect the cloud opacity, particularly for $\lambda > 2\mu\text{m}$ is shown in Fig. 14. The effect of simplifications in terms of constant particles sizes and homogeneous

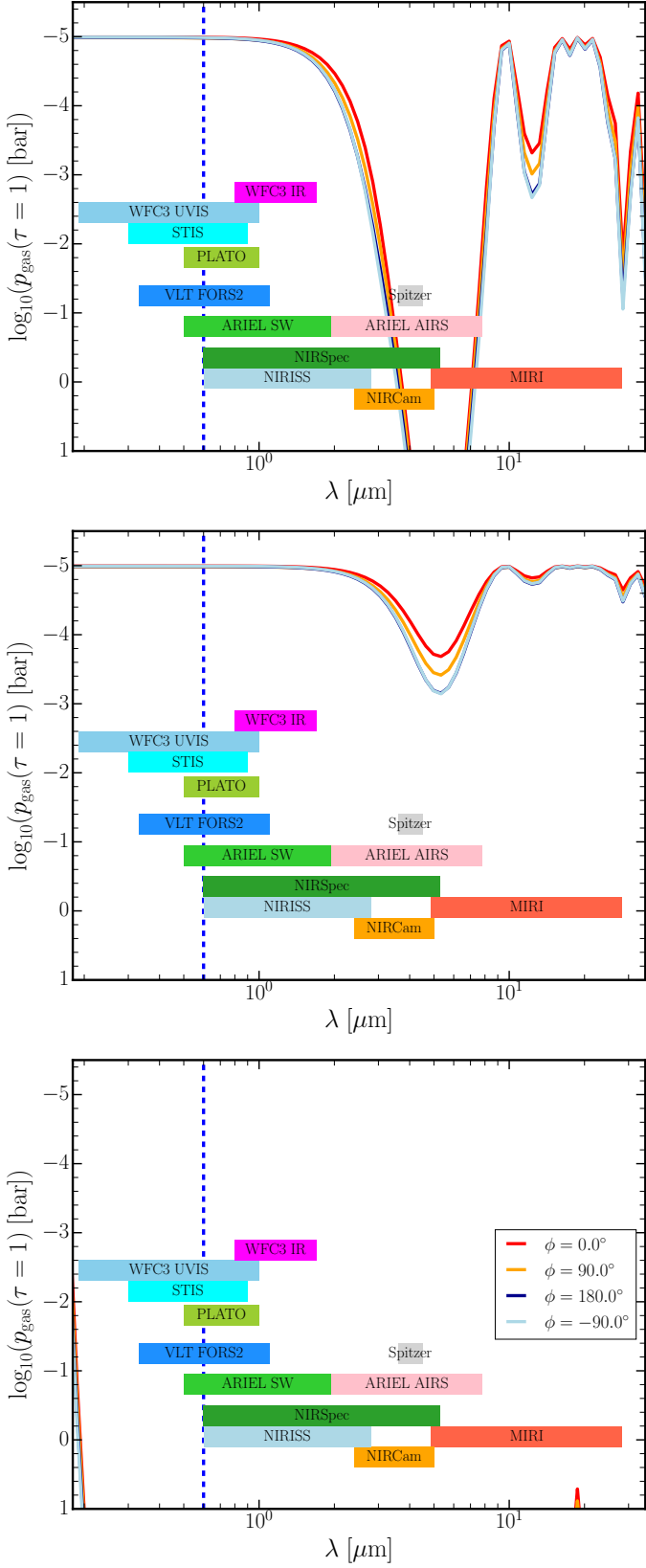


Fig. 14: Pressure levels, $p_{\text{gas}}(\tau = 1)$ [bar], at which the atmosphere becomes optically thick due to cloud opacity for WASP-39b, assuming constant, mono-disperse, cloud particles made of forsterite ($\text{Mg}_2\text{SiO}_4[\text{s}]$). **Top:** $\langle a \rangle_A = 10^{-1} \mu\text{m}$, $n_d = 10^4 \text{cm}^{-3}$, **Middle:** $\langle a \rangle_A = 10^{-1} \mu\text{m}$, $n_d = 10^5 \text{cm}^{-3}$, **Bottom:** $\langle a \rangle_A = 10^{-2} \mu\text{m}$, $n_d = 10^4 \text{cm}^{-3}$ leaving the cloud optically thin.

material properties is demonstrated. For this simplified model, two particle number densities are used ($n_d = 10^4, 10^5 \text{cm}^{-3}$), and two cloud particle sizes ($\langle a \rangle_A = 10^{-2}, 10^{-1} \mu\text{m}$). These values are based on the minimum and maximum values of cloud particle properties in the full microphysical model (Fig. 9) in the optically thin pressure range ($10^{-4.5} \dots 10^{-3}$ bar, Fig 12). Forsterite ($\text{Mg}_2\text{SiO}_4[\text{s}]$) was chosen as it is the largest volume constituent of the cloud particles in the optically thin pressure range (Fig. 7).

The spectral fingerprint of the single material $\text{Mg}_2\text{SiO}_4[\text{s}]$ becomes very apparent for small mean particle sizes of $0.1 \mu\text{m}$ a small cloud particle number density of 10^4cm^{-3} and diminishes with increasing number density of cloud particles (middle, 10^5cm^{-3}).

With $\langle a \rangle_A = 10^{-1} \mu\text{m}$, clouds are more optically thick than in the full microphysical case explored so far. However, even in such an optically thick case, ‘windows’ that allow to observe deeper parts of the atmosphere can appear for different cloud particle compositions. For example, by assuming a full forsterite ($\text{Mg}_2\text{SiO}_4[\text{s}]$) composition, there are optically thinner ‘windows’ both between the 8 and 18 μm silicate features. But also a completely optically thin (down to at least 10^2 bar, not shown) window in the near- and mid-infrared ($\sim 4 \dots 7 \mu\text{m}$) for the lower number density case ($n_d = 10^4 \text{cm}^{-3}$).

If instead a pure $\text{Fe}_2\text{SiO}_4[\text{s}]$ or pure $\text{MgSiO}_3[\text{s}]$ composition is assumed, the infrared spectral features would be very different (Fig. 15) because of the clearly different refractory indices (Fig B.1). In particular, pure $\text{Fe}_2\text{SiO}_4[\text{s}]$ cloud particles do not show the optically thin window at $\sim 4 \dots 7 \mu\text{m}$, as is the case for $\text{Mg}_2\text{SiO}_4[\text{s}]$ and $\text{MgSiO}_3[\text{s}]$. This wavelength regime is especially sensitive to cloud material composition, size, and number density. There is a particular sensitivity between iron and magnesium silicates.

In addition, for wavelengths $> 7 \mu\text{m}$ there is substantial differences between the features of all of the materials. As the cloud particles in the observable atmosphere are highly mixed (see Table 1), a simple model with this constant composition is also shown (Fig. 15, bottom). From this, the mixing of infrared features between all the materials involved (including Fe[s]) can be readily seen, and hence the lack of an optically thin window in the full material composition optical depth (Fig. 12).

The bottom of Fig. 14 shows that the $\tau = 1$ level of the clouds is also very sensitive to particle size ($\langle a \rangle_A \sim 10^{-2} \mu\text{m}$). In this instance because of both the changing total cloud mass in this simplified model, but also Rayleigh scattering as discussed in Section 4.2. The changing particle size with pressure is what causes the slope in optically thick pressure level; at different wavelengths, different depths in the atmosphere are where the cloud particles change scattering regime (from Rayleigh to Mie).

Taken together, what this simplified approach shows is the biases that are introduced when reducing the complexity of cloud particle size, number density, and material composition. As observational data across a broader wavelength range becomes available, problems may occur with the patchiness of the of the clouds. The sensitivity of near- and mid-infrared observations to the Fe/Mg composition of silicate cloud particles, which is being discussed for substellar atmospheres (e.g. Wakeford & Sing 2015; Luna & Morley 2021; Burningham et al. 2021), is also difficult to assess without taking into account the possibility of highly-mixed composition. Fits using parameterised cloud opacities for material composition (Kitzmann & Heng 2018; Taylor et al. 2021) will be challenged by the mixed material composition of clouds, which changes with height in the atmosphere. Furthermore, retrievals of the same JWST/NIRSpec G395H ($3 \dots 5 \mu\text{m}$) observations of WASP-39b yield differing

values of metallicity when specific condensate clouds are modelled in comparison to a grey cloud deck (Alderson et al. 2022).

5. Conclusion

WASP-39b, similar to WASP-96b, is cool enough that clouds are expected to form globally. A cloud-free atmosphere with $> 100 \times \epsilon_{\text{solar}}$, as implied by previous studies for this planet (Wakeford et al. 2018), is thus not consistent with the high efficiency of cloud formation in this temperature range. A cloudy and $\sim 10 \times \epsilon_{\text{solar}}$ atmosphere provides a better fit, consistent with recent JWST observations. We thus suggest that retrievals should add a cloud model by default.

Application of a non-equilibrium cloud formation model further elucidates that simple grey cloud models - as used in atmosphere retrieval - do not capture the mixed composition cloud particles which are expected to form in the WASP-39b atmosphere. The cloud composition will vary throughout the atmosphere in response to the changing local thermodynamic conditions. Inclusion of the varying composition of clouds in exoplanet atmospheres may be required to fully interpret the wealth of observational data that is offered by current and future JWST observations.

The following points summarise the findings on the atmosphere structure and cloud composition of WASP-39b, as well as highlighting the care that is needed in interpreting simple cloud models used in retrievals:

- Hydrodynamic redistribution of irradiated heating is efficient enough in such cool objects that day-night temperature differences are not very large, therefore, WASP-39b is expected to be homogeneously covered in clouds.
- The terminators inherit a temperature similar to either one hemisphere, the morning terminator is similar to the nightside and the evening terminator is similar to the dayside. Hence, trends in cloud properties at the terminators of WASP-39b are divergent between the terminators and similar to the influencing hemisphere.
- Cooler temperatures in Rossby vortices at the nightside increase cloud formation compared to other locations at the same pressure level.
- The cloud composition in this temperature regime can be very heterogeneous, leading to vertical patchiness in terms of material composition. The cloud deck is characterised by an almost equal mixture of silicates and metal oxides, with a small fraction of high temperature condensates. The deeper atmosphere is dominated by an extended silicate cloud layer and a high temperature condensate cloud base.
- Increased atmospheric metallicity enhances cloud mass and stabilises the deep extended silicate cloud layer to higher pressures.
- Increased metallicity does not qualitatively change the expectation of mixed composition upper cloud layers.
- Sulphur may be used to trace planet formation processes more easily than Fe, Mg, Si or even O since it is considerably less affected by condensation processes.
- Similar to WASP-96b (Samra et al. 2022), a reduced vertical mixing by approximately two orders of magnitude may be required to explain a cloud deck between 5×10^{-3} bar and 1×10^{-2} bar in a $10 \times \epsilon_{\text{solar}}$ metallicity WASP-39b atmosphere.
- Simplification of cloud microphysical properties can lead to biases in retrieval. These simplifications are: neglecting the

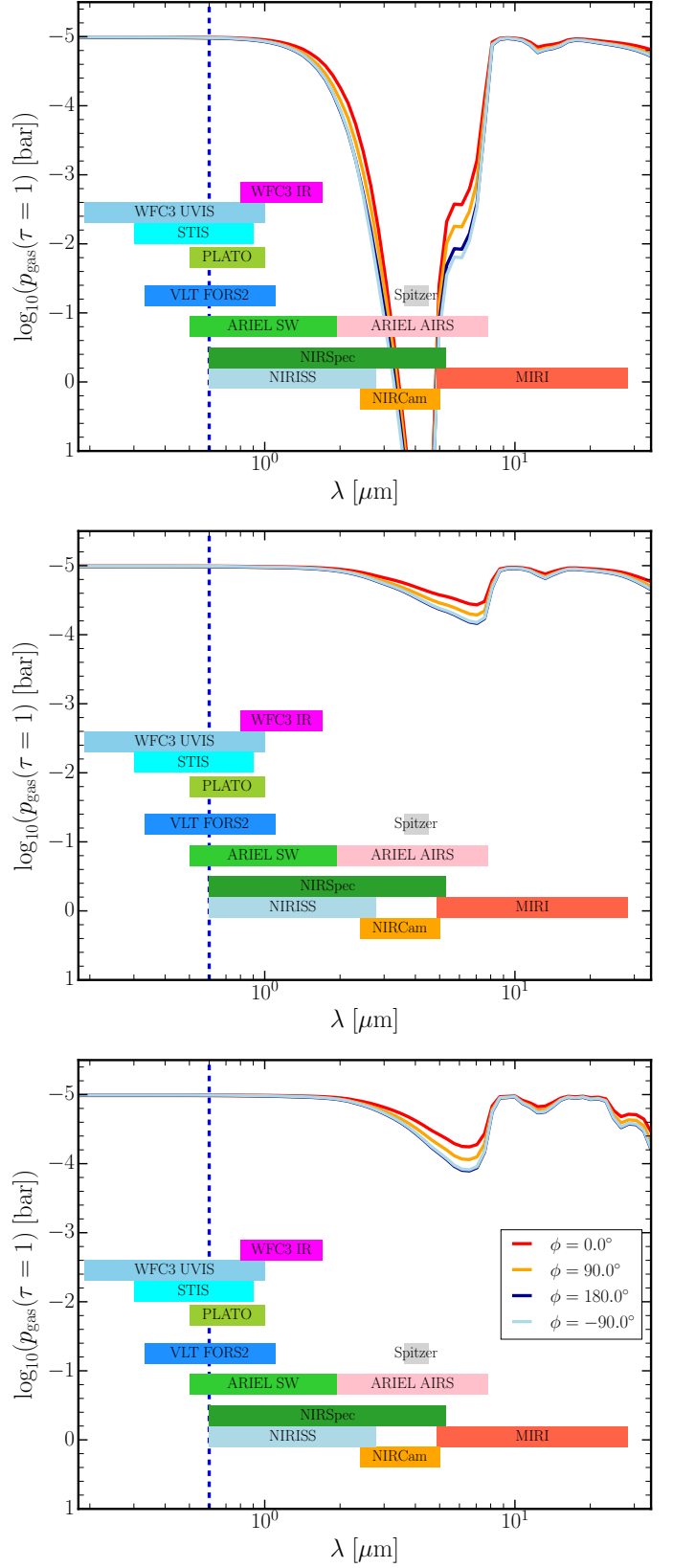


Fig. 15: Pressure levels, $p_{\text{gas}}(\tau(\lambda) = 1)$ [bar], at which the atmosphere becomes optically thick due to cloud opacity for WASP-39b, assuming constant, mono-disperse, cloud particles for various materials, where $\langle a \rangle_A = 10^{-1} \mu\text{m}$, $n_d = 10^4 \text{cm}^{-3}$ (comparable to the top of Fig. 14). **Top:** For cloud particles made of $\text{MgSiO}_3[\text{s}]$. **Middle:** For cloud particles made of $\text{Fe}_2\text{SiO}_4[\text{s}]$. **Bottom:** Mixed cloud composition based on $p_{\text{gas}} = 2 \times 10^{-4}$ bar, see Table 1.

pressure dependence of cloud particle size and number density. Further, a highly mixed material composition has a profound impact on cloud optical depth and observations. Understanding these biases will be especially crucial for near- and mid-infrared observations with JWST.

It is promising that adjustment of vertical mixing alone by the same factor yields for the complex model already good agreement with both, the WASP-96b and here the WASP-39b data. Thus, this work indicates that the microphysical cloud model can be adjusted using the new JWST data to yield better predictions of future observations and to act as a physically motivated background model to guide atmospheric retrievals.

Acknowledgements. D.A.L. and D.S. acknowledge financial support from the Austrian Academy of Sciences. Ch.H., L.C. and A.D.S. acknowledge funding from the European Union H2020-MSCA-ITN-2019 under Grant Agreement no. 860470 (CHAMELEON).

References

- Adcroft, A., Campin, J.-M., Hill, C., & Marshall, J. 2004, *Monthly Weather Review*, 132, 2845
- Agúndez, M., Biver, N., Santos-Sanz, P., Bockelée-Morvan, D., & Moreno, R. 2014, *A&A*, 564, L2
- Ahrer, E.-M., Stevenson, K. B., Mansfield, M., et al. 2022, *Early Release Science of the exoplanet WASP-39b with JWST NIRCAM*
- Alderson, L., Wakeford, H. R., Alam, M. K., et al. 2022, *Early Release Science of the Exoplanet WASP-39b with JWST NIRSpec G395H*
- Allard, N. F., Spiegelman, F., & Kielkopf, J. F. 2016, *A&A*, 589, A21
- Allard, N. F., Spiegelman, F., Leininger, T., & Mollière, P. 2019, *A&A*, 628, A120
- Atreya, S. K., Crida, A., Guillot, T., et al. 2016, *arXiv e-prints*, arXiv:1606.04510
- Azzam, A. A. A., Tennyson, J., Yurchenko, S. N., & Naumenko, O. V. 2016, *Monthly Notices of the Royal Astronomical Society*, 460, 4063
- Baeyens, R., Decin, L., Carone, L., et al. 2021, *MNRAS*, 505, 5603
- Barstow, J. K., Aigrain, S., Irwin, P. G. J., & Sing, D. K. 2017, *ApJ*, 834, 50
- Begemann, B., Dorschner, J., Henning, T., et al. 1997, *ApJ*, 476, 199
- Burningham, B., Faherty, J. K., Gonzales, E. C., et al. 2021, *MNRAS*, 506, 1944
- Carone, L., Baeyens, R., Mollière, P., et al. 2020, *MNRAS*, 496, 3582
- Carone, L., Mollière, P., Zhou, Y., et al. 2021a, *A&A*, 646, A168
- Carone, L., Mollière, P., Zhou, Y., et al. 2021b, *A&A*, 646, A168
- Chachan, Y., Knutson, H. A., Gao, P., et al. 2019, *AJ*, 158, 244
- Colavitti, E., Cescutti, G., Matteucci, F., & Murante, G. 2009, *A&A*, 496, 429
- Danilovich, T., De Beck, E., Black, J. H., Olofsson, H., & Justtanont, K. 2016, *A&A*, 588, A119
- Danilovich, T., Ramstedt, S., Gobrecht, D., et al. 2018, *A&A*, 617, A132
- Danilovich, T., Richards, A. M. S., Decin, L., Van de Sande, M., & Gottlieb, C. A. 2020, *MNRAS*, 494, 1323
- Danilovich, T., Van de Sande, M., De Beck, E., et al. 2017, *A&A*, 606, A124
- Dorschner, J., Begemann, B., Henning, T., Jaeger, C., & Mutschke, H. 1995, *A&A*, 300, 503
- Faedi, F., Barros, S. C. C., Anderson, D. R., et al. 2011, *A&A*, 531, A40
- Feinstein, A. D., Radica, M., Welbanks, L., et al. 2022, *Early Release Science of the exoplanet WASP-39b with JWST NIRISS*
- Fischer, P. D., Knutson, H. A., Sing, D. K., et al. 2016, *ApJ*, 827, 19
- Fletcher, L. N., Baines, K. H., Momary, T. W., et al. 2011, *Icarus*, 214, 510
- Fortney, J. J., Visscher, C., Marley, M. S., et al. 2020, *AJ*, 160, 288
- Gobrecht, D., Cherchneff, I., Sarangi, A., Plane, J. M. C., & Bromley, S. T. 2016, *A&A*, 585, A6
- Guillot, T. 2010, *A&A*, 520, A27
- Guillot, T., Fletcher, L. N., Helled, R., et al. 2022, *arXiv e-prints*, arXiv:2205.04100
- Hellier, C., Anderson, D. R., Cameron, A. C., et al. 2014, *Monthly Notices of the Royal Astronomical Society*, 440, 1982
- Helling, Ch. 2019, *Annual Review of Earth and Planetary Sciences*, 47, 583
- Helling, Ch., Gourbin, P., Woitke, P., & Parmentier, V. 2019a, *A&A*, 626, A133
- Helling, Ch., Iro, N., Corrales, L., et al. 2019b, *A&A*, 631, A79
- Helling, Ch., Kawashima, Y., Graham, V., et al. 2020, *A&A*, 641, A178
- Helling, Ch., Lee, E., Dobbs-Dixon, I., et al. 2016, *MNRAS*, 460, 855
- Helling, Ch., Lewis, D., Samra, D., et al. 2021, *A&A*, 649, A44
- Helling, Ch., Samra, D., Lewis, D., et al. 2022, *arXiv e-prints*, arXiv:2208.05562
- Henning, T., Begemann, B., Mutschke, H., & Dorschner, J. 1995, *A&AS*, 112, 143
- Kataria, T., Showman, A. P., Lewis, N. K., et al. 2013, *ApJ*, 767, 76
- Kitzmann, D. & Heng, K. 2018, *MNRAS*, 475, 94
- Knierim, H., Shibata, S., & Helled, R. 2022, *A&A*, 665, L5
- Kreidberg, L., Line, M. R., Parmentier, V., et al. 2018, *AJ*, 156, 17
- Lee, E., Dobbs-Dixon, I., Helling, Ch., Bogner, K., & Woitke, P. 2016, *A&A*, 594, A48
- Lee, E., Helling, Ch., Dobbs-Dixon, I., & Juncher, D. 2015, *A&A*, 580, A12
- Line, M. R. & Parmentier, V. 2016, *ApJ*, 820, 78
- Luna, J. L. & Morley, C. V. 2021, *ApJ*, 920, 146
- Mahapatra, G., Helling, Ch., & Miguel, Y. 2017, *MNRAS*, 472, 447
- Min, M., Ormel, C. W., Chubb, K., Helling, Ch., & Kawashima, Y. 2020, *A&A*, 642, A28
- Molaverdikhani, K., Helling, Ch., Lew, B. W. P., et al. 2020, *A&A*, 635, A31
- Mollière, P., Wardenier, J. P., van Boekel, R., et al. 2019, *A&A*, 627, A67
- Moses, J. I., Visscher, C., Fortney, J. J., et al. 2011, *The Astrophysical Journal*, 737, 15
- Nikolov, N., Sing, D. K., Gibson, N. P., et al. 2016, *The Astrophysical Journal*, 832, 191
- Ormel, C. W. & Min, M. 2019, *A&A*, 622, A121
- Palik, E. D. 1985, *Handbook of optical constants of solids* (Academic Press)
- Perdigon, J., de Laverny, P., Recio-Blanco, A., et al. 2021, *A&A*, 647, A162
- Pinhas, A., Madhusudhan, N., Gandhi, S., & MacDonald, R. 2019, *MNRAS*, 482, 1485
- Posch, T., Kerschbaum, F., Fabian, D., et al. 2003, *ApJS*, 149, 437
- Reyniers, M. & van Winkel, H. 2007, *A&A*, 463, L1
- Rothman, L. S., Gordon, I. E., Barber, R. J., et al. 2010, *JQSRT*, 111, 2139
- Rustamkulov, Z., Sing, D. K., Mukherjee, S., et al. 2022, *Early Release Science of the exoplanet WASP-39b with JWST NIRSpec PRISM*
- Samra, D., Helling, Ch., Chubb, K., et al. 2022, *arXiv e-prints*, arXiv:2211.00633
- Schneider, A. D. & Bitsch, B. 2021, *A&A*, 654, A71
- Schneider, A. D., Carone, L., Decin, L., et al. 2022a, *arXiv e-prints*, arXiv:2202.09183
- Schneider, A. D., Carone, L., Decin, L., Jørgensen, U. G., & Helling, Ch. 2022b, *A&A*, 666, L11
- Sharp, C. M. & Burrows, A. 2007, *ApJS*, 168, 140
- Sing, D. K., Fortney, J. J., Nikolov, N., et al. 2016, *Nature*, 529, 59
- Suto, H., Sogawa, H., Tachibana, S., et al. 2006, *MNRAS*, 370, 1599
- Taylor, J., Parmentier, V., Line, M. R., et al. 2021, *MNRAS*, 506, 1309
- The JWST Transiting Exoplanet Community Early Release Science Team, Ahrer, E.-M., Alderson, L., et al. 2022, *arXiv e-prints*, arXiv:2208.11692
- Thorngren, D. & Fortney, J. J. 2019, *ApJL*, 874, L31
- Tsai, S.-M., Lee, E. K. H., Powell, D., et al. 2022, *Direct Evidence of Photochemistry in an Exoplanet Atmosphere*
- Venot, O., Hébrard, E., Agúndez, M., et al. 2012, *Astronomy & Astrophysics*, 546, A43
- Waelkens, C., Van Winkel, H., Bogaert, E., & Trams, N. R. 1991, *A&A*, 251, 495
- Wakeford, H. R. & Sing, D. K. 2015, *A&A*, 573, A122
- Wakeford, H. R., Sing, D. K., Deming, D., et al. 2018, *AJ*, 155, 29
- Welbanks, L., Madhusudhan, N., Allard, N. F., et al. 2019, *ApJL*, 887, L20
- Woitke, P., Helling, Ch., Hunter, G. H., et al. 2018, *A&A*, 614, A1
- Yurchenko, S. N., Mellor, T. M., Freedman, R. S., & Tennyson, J. 2020, *Monthly Notices of the Royal Astronomical Society*, 496, 5282
- Zahnle, K., Marley, M. S., Freedman, R. S., Lodders, K., & Fortney, J. J. 2009, *The Astrophysical Journal*, 701, L20
- Zeidler, S., Posch, T., & Mutschke, H. 2013, *A&A*, 553, A81
- Zeidler, S., Posch, T., Mutschke, H., Richter, H., & Wehrhan, O. 2011, *A&A*, 526, A68

Appendix A: GCM parameters and additional details

Table A.1: Model parameters for the GCM used to produce 1D profiles for WASP-39b

Parameter	Value
Dynamical time-step Δt	25 s
Radiative time-step Δt_{rad}	100 s
Stellar Temperature ¹ (T_*)	5400 K
Stellar Radius ¹ (R_*)	$0.895 R_{\text{sun}}$
Semi-major axis ¹ (a_p)	0.0486 au
Substellar irradiation temperature ² (T_{irr})	1580 K
Equilibrium temperature ² (T_{eq})	1117 K
Planetary Radius ¹ (R_p)	$1.27 R_{\text{Jup}}$
Specific heat capacity at constant pressure ³ (c_p)	$13165 \text{ J kg}^{-1} \text{ K}^{-1}$
Specific gas constant ³ (R)	$3456 \text{ J kg}^{-1} \text{ K}^{-1}$
Rotation period (P_{rot})	4.06 days
Surface gravity (g)	430 cm s^{-2}
Lowest pressure (p_{top})	10^{-5} bar
Highest pressure (p_{bottom})	700 bar
Vertical Resolution (N_{layers})	47
Wavelength Resolution ⁴ (S1)	11

Notes: 1. Values taken from Faedi et al. (2011), 2. Calculated using Eq. 1 from Guillot (2010), 3. Inferred using petitRADTRANS equilibrium package for $10\times$ solar metallicity, 4. Same as Kataria et al. (2013) benchmarked in Appendix B. Schneider et al. (2022a)

Appendix B: Cloud Condensate Refractive Indices

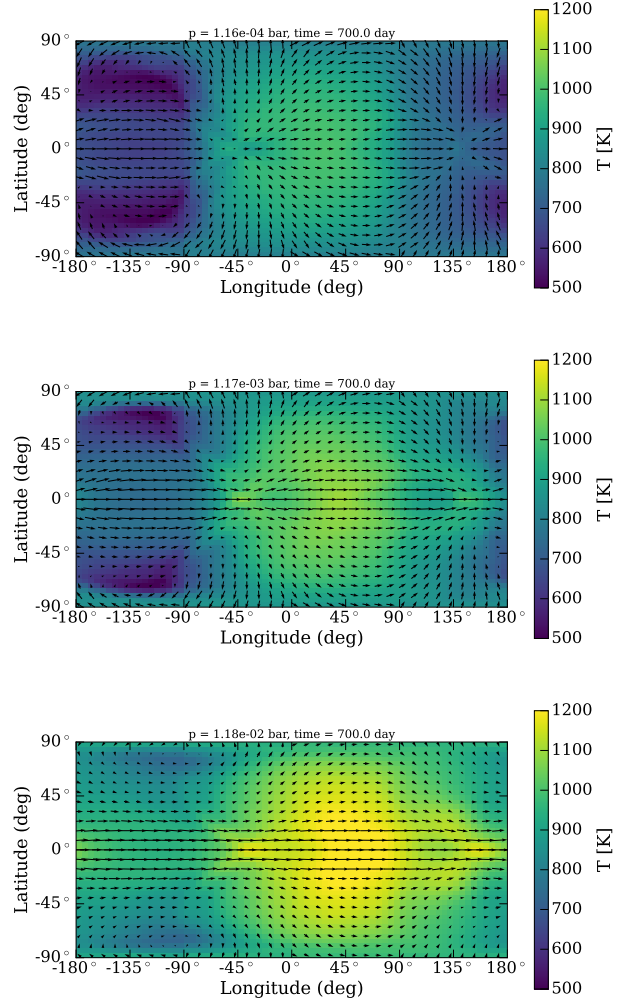


Fig. A.1: Isobaric maps of average gas temperature for $p_{\text{gas}} \sim 10^{-4}, 10^{-3},$ and 10^{-2} bar. The Rossby vortices are seen clearly on the nightside around latitude = 68° at the $p_{\text{gas}} \sim 10^{-4}$ and 10^{-3} bar levels. **Top:** $p_{\text{gas}} \sim 10^{-4}$ bar. **Middle:** $p_{\text{gas}} \sim 10^{-3}$ bar. **Bottom:** $p_{\text{gas}} \sim 10^{-2}$ bar

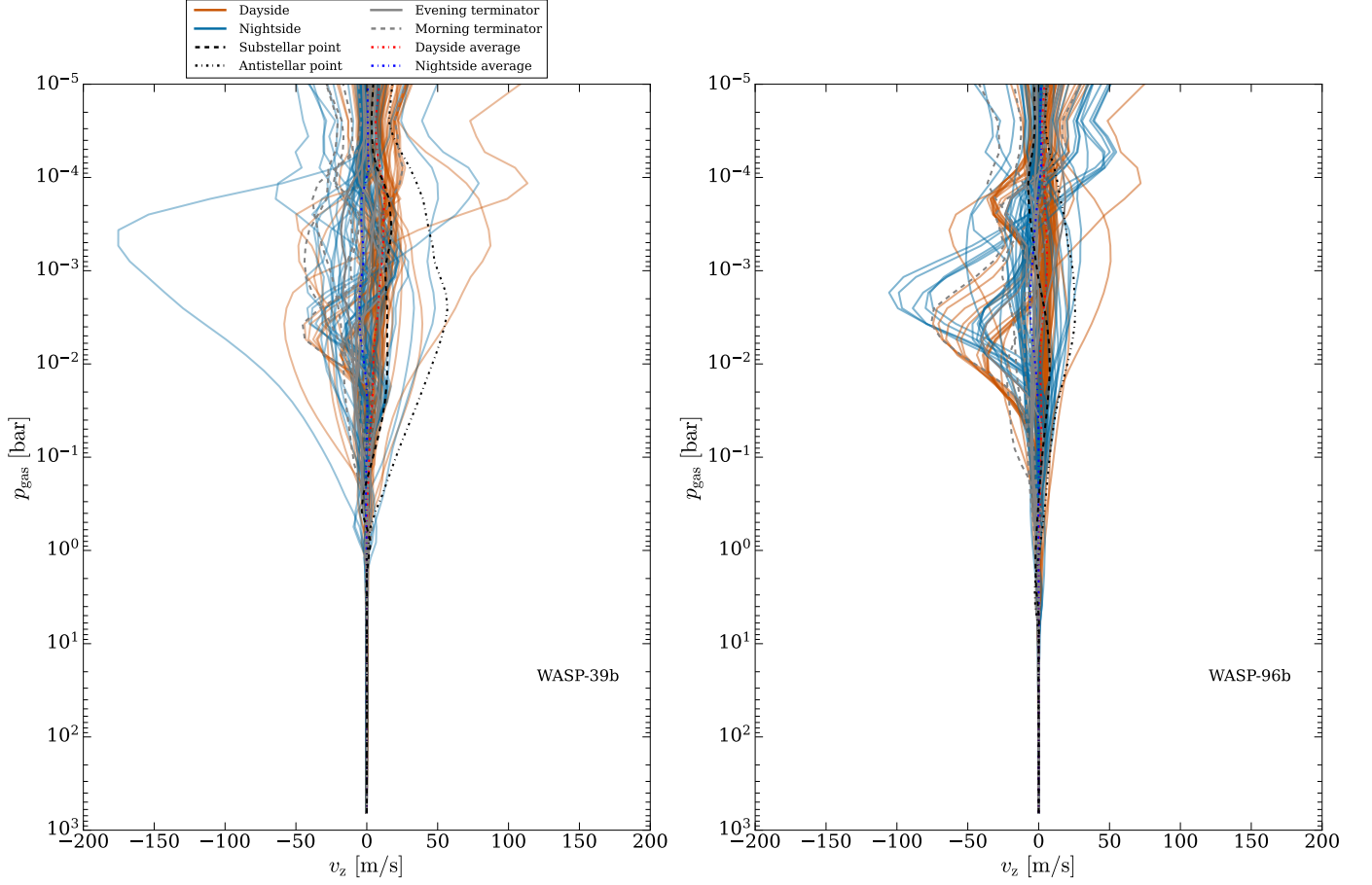


Fig. A.2: (v_z, p_{gas}) -profiles extracted from the 3D GCM. **Left:** WASP-39b. **Right:** WASP-96b

Table B.1: Cloud condensate refractive indices wavelength coverage and sources

Material Species	Reference	Wavelength Range (μm)
TiO ₂ [s] (rutile)	Zeidler et al. (2011)	0.47–36
SiO ₂ [s] (alpha-Quartz)	Palik (1985), Zeidler et al. (2013)	0.00012–10000
SiO[s] (polycrystalline)	Philipp in Palik (1985)	0.0015–14
MgSiO ₃ [s] (glass)	Dorschner et al. (1995)	0.20–500
Mg ₂ SiO ₄ [s] (crystalline)	Suto et al. (2006)	0.10–1000
MgO[s] (cubic)	Palik (1985)	0.017–625
Fe[s] (metallic)	Palik (1985)	0.00012–285
FeO[s] (amorphous)	Henning et al. (1995)	0.20–500
Fe ₂ O ₃ [s] (amorphous)	Amaury H.M.J. Triaud (unpublished)	0.10–1000
Fe ₂ SiO ₄ [s] (amorphous)	Dorschner et al. (1995)	0.20–500
FeS[s] (amorphous)	Henning (unpublished)	0.10–100000
CaTiO ₃ [s] (amorphous)	Posch et al. (2003)	2–5843
CaSiO ₃ [s]	No data - treated as vacuum	N/A
Al ₂ O ₃ [s] (glass)	Begemann et al. (1997)	0.10–200
C[s] (graphite)	Palik (1985)	0.20–794

Notes:

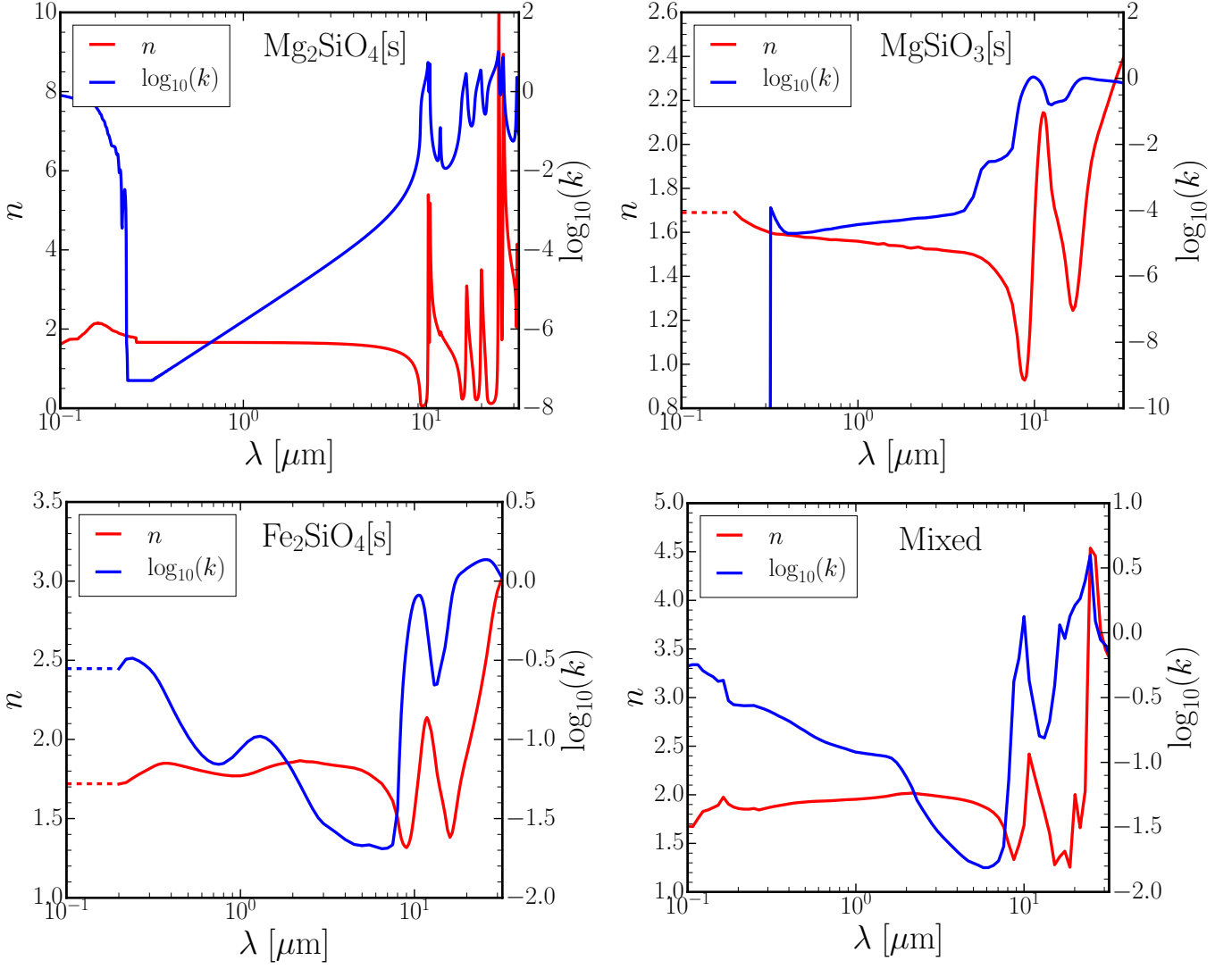


Fig. B.1: Refractive indices of silicate materials used **Top Left:** forsterite ($\text{Mg}_2\text{SiO}_4[\text{s}]$), **Top right:** enstatite (MgSiO_3), **Bottom left:** fayalite ($\text{Fe}_2\text{SiO}_4[\text{s}]$), **Bottom right:** mixed composition cloud based on $p_{\text{gas}} = 2 \times 10^{-4}$ bar, see Table 1. Dashed lines indicate regions for which refractive indices were extrapolated. Extrapolation was done as according to Lee et al. (2016).